IEEE Journal of Emerging and Selected Topics in Power Electronics (JESTPE), Vol. 13, No. 1, pp. 72-90, February 2025

Optimal Space Vector Modulation of a New Bidirectional Dual-Active-Bridge-Type Single-Stage Isolated Three-Phase Buck-Boost PFC Rectifier System

F. Krismer,
D. Menzi,
P. Ziegler,
A. Yang,
J. W. Kolar

This article has been accepted for publication in IEEE Journal of Emerging and Selected Topics in Power Electronics. This is the author's version which has not been fully edited and content may change prior to final publication. Citation information: DOI 10.1109/JESTPE.2024.3475826

Optimal Space Vector Modulation of a New Bidirectional Dual-Active-Bridge-Type Single-Stage Isolated Three-Phase Buck-Boost PFC Rectifier System

Florian Krismer, David Menzi, Patrick Ziegler, Aobo Yang, Johann W. Kolar
Power Electronic Systems Laboratory, ETH Zurich, Switzerland
krismer@lem.ee.ethz.ch

Dedicated to Prof. Ned Mohan, who established the basis for the space-vector-based analysis of the category of single-stage ac–dc converter structures investigated in this work.

***Abstract*—This paper describes the optimization of a modulation scheme for the isolated Y-Rectifier (iYR), a bidirectional three-phase PFC rectifier with integrated galvanic isolation, with regard to minimum rms values of the transformer currents. The optimization is based on a numerical method, which utilizes Space Vector (SV) calculation to determine the steady-state waveforms of the iYR's transformer currents with low computational effort. Compared to an existing modulation method, the optimization results show that, at part load operation, a substantial reduction of the transformer rms current is achieved. For example, the experimental results confirm that the optimization enables a reduction of the rms value of the transformer current SV over a grid period from $11.1\,\mathrm{A}$ to $8.8\,\mathrm{A}$ at a three-phase grid voltage of $400\,\mathrm{V}$ (rms, line-to-line), a dc output voltage of $400\,\mathrm{V}$, and an output power of $1.2\,\mathrm{kW}$ (equal to $20\,\%$ of the rated power of $6\,\mathrm{kW}$). Owing to the generalized consideration of the iYR made possible by the space-vector-based description, the obtained optimization results can be applied directly also to other rectifier topologies presented in this paper. This and further results and methods described in this paper reveal the potential of SV calculation in connection with comprehensive analyses of complex three-phase isolated PFC rectifier systems.**

I. Introduction

Three-phase power factor correction (PFC) rectifiers with galvanic isolation are used in various applications, e.g., solid-state transformers [2], [3], photovoltaic power systems [4]–[6] and energy storage systems [7], [8], more electric aircraft [9], mains interfaces of dc microgrids [10], and battery chargers for electric vehicles (EV) [11]–[13]. This paper considers an isolated PFC rectifier for an EV battery charging application, which is realized by the single-stage, isolated ac–dc converter structure depicted in Fig. 1(a). The system operating voltages and currents have been determined on the basis of the specifications given in [14] and are summarized in Tab. I.

In a conventional approach, a two-stage circuit would be typically used to realize three-phase PFC ac–dc conversion (first stage) and galvanic isolation (second stage) [15]–[17].

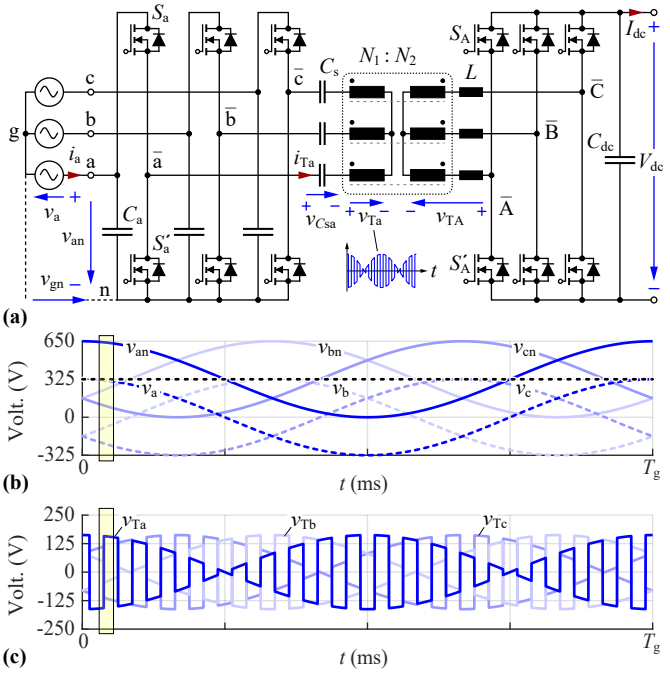

Fig. 1: (a) iYR proposed in [1]. (b), (c) Simulated waveforms of $v_{\{a,b,c\}n}$, $v_{\{a,b,c\}}$, and $v_{T\{a,b,c\}}$ of the iYR for operation according to Tab. I except for $f_s = 1\,\mathrm{kHz}$. The yellow area marks $\phi_g \approx 15°$, which has been used to create Fig. 4.

TABLE I: Considered specifications and converter settings.

Designator	Description	Value
V_g	Grid voltage (line to neutral, rms)	$3 \times 230\,\mathrm{V}$
I_g	Grid phase current (rms)	$3 \times 10\,\mathrm{A}$
$f_g = T_g^{-1}$	Grid frequency, grid period	$50\,\mathrm{Hz}$, $20\,\mathrm{ms}$
P_{nom}	Nominal power	$6\,\mathrm{kW}$
$V_{dc,min}$	Minimum dc voltage	$200\,\mathrm{V}$
$V_{dc,max}$	Maximum dc voltage	$750\,\mathrm{V}$
$I_{dc,max}$	Maximum dc current	$15\,\mathrm{A}$
$f_s = T_s^{-1}$	Switching frequency, switching period	$72\,\mathrm{kHz}$, $13.9\,\mu\mathrm{s}$
$n = N_1 : N_2$	Transformer turns ratio	1
L	Series inductance	$14\,\mu\mathrm{H}$

With the aim of counteracting the disadvantage of multiple energy conversions, single-stage concepts that combine sinusoidal input current shaping (PFC), galvanic isolation, and rectification are increasingly being presented.

Three-phase single-stage concepts for ac–dc converters can be divided into phase-modular concepts that are based on three single-phase converters [18]–[21], non-modular concepts with only one high-frequency (hf) transformer [22]–[26], and non-modular concepts with three hf transformers (or one three-phase hf transformer) [1], [27]–[30]. The single-phase ac–dc converters used in phase-modular concepts are typically extended versions of dc–dc converters with galvanic isolation, e.g., dual active bridge (DAB) converters [18], [19], multilevel converters [20], or series resonant converters [21]. However, the advantage of complete modularity is opposed by the disadvantage of a comparatively high number of components. A reduction of the number of components is achieved by non-modular converter topologies. Such topologies with only one hf transformer often use a matrix converter on the ac side [22]–[24], but other topologies are also conceivable, such as the topology presented in [25], which is variant of the VIENNA rectifier II topology [26] that has been extended to enable bidirectional operation. Numerous publications also exist for non-modular topologies with three hf transformers. Examples are the quad active bridge converter presented in [27] and the converters with dc-side six-switch rectifiers presented in [1], [28], [29].

The converter presented in [28], [29] has the advantage of using only two transistors on the primary side. Disadvantages are high switching voltage stress on the transistors and the need for primary-side transformer windings with center taps. These disadvantages are mitigated by the second circuit, which is shown in **Fig. 1(a)** and presented in [1]. This second topology is referred to as isolated Y-Rectifier (iYR) and is the topology considered in this paper. Although the iYR requires six instead of two transistors on the primary side, fewer transistors are still required overall compared to most other non-modular topologies (e.g., the matrix converter-based topology, which in total employs 16 transistors [24]). Furthermore, in contrast to matrix converters, the switching state changes are carried out without following a special multi-step procedure (except for maintaining a certain dead time). Note that primary-side capacitors are connected in series with the hf transformers to ensure zero local average values (the average over one switching period) of the hf ac voltages applied to the transformer windings.

Interestingly, further realization variants can be found for the ac side of the converter under investigation. Two examples are presented in [30]. One topology presented there is a realization with full bridges on the ac side. Compared to the circuit shown in Fig. 1(a), this allows a reduction of the maximum reverse voltages across the primary-side switches to almost one half. The second realization shown in [30] allows the use of the monolithic bidirectional GaN switches described in [31] and expectedly facilitates lower conduction losses.

The circuit depicted in Fig. 1(a) and the circuits presented in [28]–[30] can generate primary-side transformer voltages, which are identical apart from different amplitudes and employ the same secondary-side rectifier circuit. Consequently, the modulation scheme described in [29], which is referred to as conventional modulation scheme in this paper and summarized in **Section II**, can be applied to all these circuits. However, the conventional modulation scheme was not derived on the basis of optimization. Therefore, it is to be expected that improvements, e.g., reduced transformer winding losses or conduction losses, are achievable in certain operating regions. This motivates the detailed analysis and optimization carried out in this paper.

It is well known in the context of conventional single-phase DAB dc–dc converters which operate in wide voltage and power ranges that relatively large currents with high rms values in the hf ac path can result. This leads to relatively high conduction losses in the transistors and copper losses in the transformer, since the rms value of the current in the hf ac path is directly related to these losses [32]. In the iYR, the conduction and copper losses in transistors and transformers are directly related to the rms values of the currents in the hf ac paths as well. Since it is possible to reduce these rms values by optimizing the modulation scheme, the first step is to carry out an optimization in this respect as described in **Section III**. A discussion of the optimization results is presented in **Section IV**. However, it is found that the optimized modulation scheme not only leads to reduced rms values of the transformer currents. In addition, the functions of the optimized control parameters exhibit discontinuities that can lead to difficulties in practice (e.g. excitation of parasitic oscillations). In order to arrive at functions for the control parameters without discontinuities, a possible reduction of the degrees of freedom (DoFs) used for the optimization is investigated in **Section V**. Based on this, a suboptimal control method is identified, which achieves similar improvements as the control method optimized in Section IV in wide parts of the operating range. An experimental verification at three selected operating points presented in **Section VI** finally confirms the calculated results. **Section VII** summarizes the main findings and concludes the paper.

II. Converter Operating Principle

A suitable concept for studying the operating principle of the presented ac–dc converter is the Space Vector (SV) calculation [1], [29], [33]. **Fig. 2(a)** depicts the simplified equivalent circuit for the iYR in SV representation, assuming (ideal) hf transformers of the phases with same turns ratios $n = N_1/N_2$ and same series inductances L in the three converter phases. The two voltage sources $\underline{v}_{\mathrm{Tabc}}$ and $\underline{v}_{\mathrm{TABC}}$ refer to the voltage SVs generated by the primary-side inverter and the secondary-side six-switch rectifier, respectively. The inductance n^2L in the equivalent circuit is equal to the primary-side referenced inductance L in each converter phase in Fig. 1(a). Note that the equivalent circuit diagram of these ac–dc converters appears to be the same as the equivalent circuit diagram of the DAB dc–dc converter. The only difference is that in the case of the

ac–dc converters, the two voltage sources provide time-varying voltage SVs instead of real-valued voltages.

For a three-phase grid with sinusoidal grid voltages,

$$v_\mathrm{a} = \sqrt{2}V_\mathrm{g}\cos\left(\phi_\mathrm{g}\right), \qquad v_\mathrm{b} = \sqrt{2}V_\mathrm{g}\cos\left(\phi_\mathrm{g} - \tfrac{2\pi}{3}\right),$$
$$v_\mathrm{c} = \sqrt{2}V_\mathrm{g}\cos\left(\phi_\mathrm{g} - \tfrac{4\pi}{3}\right), \ \phi_\mathrm{g} = 2\pi f_\mathrm{g} t, \tag{1}$$

and $\underline{a} = \mathrm{e}^{\mathrm{j}\frac{2\pi}{3}}$, the grid voltage SV

$$\underline{v}_\mathrm{g} = \frac{2}{3}\left(v_\mathrm{a} + \underline{a}v_\mathrm{b} + \underline{a}^2 v_\mathrm{c}\right) = \sqrt{2}V_\mathrm{g}\,\mathrm{e}^{\mathrm{j}2\pi f_\mathrm{g} t} \tag{2}$$

results [34]. The primary-side half-bridges of the iYR are operated synchronously at the switching frequency and with a duty cycle of $50\,\%$. With this, the low-frequency (lf) mains voltages are converted to amplitude-modulated hf ac voltages, as shown in **Fig. 1(c)**. Accordingly, the voltage SV generated by the primary-side inverter is either $\underline{v}_\mathrm{Tabc} = \frac{\underline{v}_\mathrm{g}}{2}$ (high-side switches of all primary-side half-bridges are on) or $\underline{v}_\mathrm{Tabc} = -\frac{\underline{v}_\mathrm{g}}{2}$ (low-side switches of all primary-side half-bridges are on) for half a switching period.

It is well known that the secondary-side six-switch rectifier can reside in one of eight states, i.e., six active states and two freewheeling states. The six active states result in six different voltage SVs with length $\frac{2}{3}V_\mathrm{dc}$ and the freewheeling states to a SV with length 0, as shown in **Fig. 2(b)**. The designations $(S_\mathrm{a}S_\mathrm{b}S_\mathrm{c})$ and $(S_\mathrm{A}S_\mathrm{B}S_\mathrm{C})$ used for $\underline{v}_\mathrm{Tabc}$ and $\underline{v}_\mathrm{TABC}$ in Fig. 2(b) specify the switching states of the iYR's primary-side inverter and secondary-side rectifier, respectively. For example, S_A denotes the state of the secondary-side half-bridge of phase A:

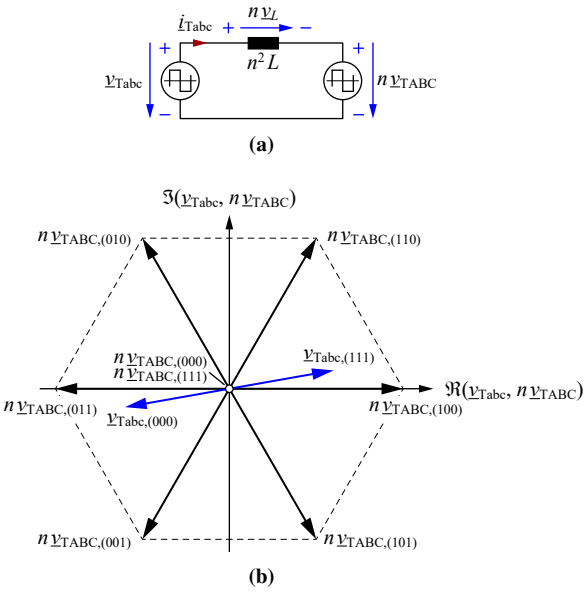

Fig. 2: (a) Equivalent circuit in Space Vector (SV) representation for the presented ac–dc converter. (b) SVs $\underline{v}_\mathrm{Tabc}$ and $\underline{v}_\mathrm{TABC}$ that can be generated by the primary-side inverter and the secondary-side rectifier of the considered ac–dc converters. Note that $(S_\mathrm{a}S_\mathrm{b}S_\mathrm{c})$ and $(S_\mathrm{A}S_\mathrm{B}S_\mathrm{C})$ used in the indexes of $\underline{v}_\mathrm{Tabc}$ and $\underline{v}_\mathrm{TABC}$ refer to the switching states of the primary-side inverter and the secondary-side rectifier, respectively.

for $S_\mathrm{A} = 0$ the switch S'_A is on and for $S_\mathrm{A} = 1$ the switch S_A is on.

Note that any common-mode voltage component present in $v_{\mathrm{T}\{\mathrm{a,b,c}\}}(t)$ has no effect on the transformer currents. This not only results from the SV calculation, but can also be easily explained using the circuit shown in **Fig. 3**. For this, it is assumed that the voltages $v_{\mathrm{T}\{\mathrm{a,b,c}\}}(t)$ are composed of differential-mode voltages $v'_{\mathrm{T}\{\mathrm{a,b,c}\}}(t)$ on which a common-mode voltage $v_\mathrm{cm}(t)$ is superimposed,

$$v_\mathrm{Ta}(t) = v'_\mathrm{Ta}(t) + v_\mathrm{cm}(t), \tag{3}$$
$$v_\mathrm{Tb}(t) = v'_\mathrm{Tb}(t) + v_\mathrm{cm}(t), \tag{4}$$
$$v_\mathrm{Tc}(t) = v'_\mathrm{Tc}(t) + v_\mathrm{cm}(t). \tag{5}$$

If it is assumed that the average values of $v'_{\mathrm{T}\{\mathrm{a,b,c}\}}(t)$ and $v_\mathrm{cm}(t)$ over a switching period are zero, the secondary-side transformer voltages $v_{\mathrm{T}\{\mathrm{A,B,C}\}}(t)$ contain the common-mode component $v_\mathrm{cm}(t)/n$. However, $v_\mathrm{cm}(t)$ has no impact on the phase-to-phase voltages that are present at the hf input of the secondary-side rectifier, e.g.,

$$v_\mathrm{TA}(t) - v_\mathrm{TB}(t) = \frac{v'_\mathrm{Ta}(t) - v_\mathrm{cm}(t) - v'_\mathrm{Tb}(t) + v_\mathrm{cm}(t)}{n} = \\ = \frac{v'_\mathrm{Ta}(t) - v'_\mathrm{Tb}(t)}{n}. \tag{6}$$

Because of this, $v_\mathrm{cm}(t)$ only has an effect on the electric potential at the star-point formed by the three secondary-side transformer windings and has no influence on the shape of the transformer currents, which is purely defined by phase voltage differences, i.e. line-to-line voltages.

The iYR described in this paper is controlled by means of SV Modulation (SVM). A typical form of SVM is the SVPWM, which is often used for rectifiers and inverters, as for example described in [25], [35]. With SVPWM, the voltage formation of the converters is analyzed using the SVs that are assigned to the individual switching states. Based on this, the set of SVs that form the average reference SV and the associated relative durations during which each SV is present during a switching period are determined. Hence, this determines the pulse pattern or the PWM of the phase voltages. Further forms of SVMs are presented in [36], e.g. predictive current control, which aims to minimize the deviation between the reference current SV and the grid current SV. The use of

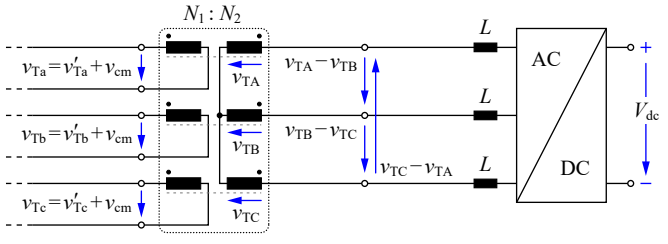

Fig. 3: The presence of a primary-side common-mode voltage $v_\mathrm{cm}(t)$ does not affect the input voltages of the rectifier on the secondary side, e.g., $v_\mathrm{TA} - v_\mathrm{TB} = (v'_\mathrm{Ta} - v'_\mathrm{Tb})/n$. Therefore, $v_\mathrm{cm}(t)$ does not affect the transformer currents.

SVM has also been proposed in the field of three-phase DAB dc–dc converters, e.g. for suppressing the average value of the magnetic flux in the magnetic core of a transformer [33].

Another form of SVM is used in the converters described in [28], [37]. This modulation scheme is not specifically optimized, is comparatively simple, and still enables an almost sinusoidal grid current. Since the iYR has the same equivalent circuit diagram as the converter described in [28], the same modulation scheme can also be applied to the iYR. Therefore, this modulation scheme, which is explained in more detail in the following, serves as the starting point for the optimization presented in this paper. For example, for $0° \leq \phi_\mathrm{g} < 60°$ the secondary-side three-phase rectifier uses the switching state sequence

$$\begin{aligned}&(000) \underset{t_\mu=t_{\mu1}}{\rightarrow} (100) \underset{t_\mu=t_{\mu2}}{\rightarrow} (110) \underset{t_\mu=t_{\mu3}}{\rightarrow} (100) \underset{t_\mu=t_{\mu4}}{\rightarrow}\\ &(000) \underset{t_\mu=t_{\mu5}}{\rightarrow} (001) \underset{t_\mu=t_{\mu6}}{\rightarrow} (011) \underset{t_\mu=t_{\mu7}}{\rightarrow} (001) \underset{t_\mu=t_{\mu8}}{\rightarrow}\\ &(000)\ldots\end{aligned} \tag{7}$$

during a switching period. Here t_μ denotes the time within a switching period and $t_{\mu i}$ the individual switching times. Note that in a symmetrical three-phase grid, the analysis can be confined to $0° \leq \phi_\mathrm{g} < 60°$ since the results in the other 60° sectors of a grid period can be derived from this [29].

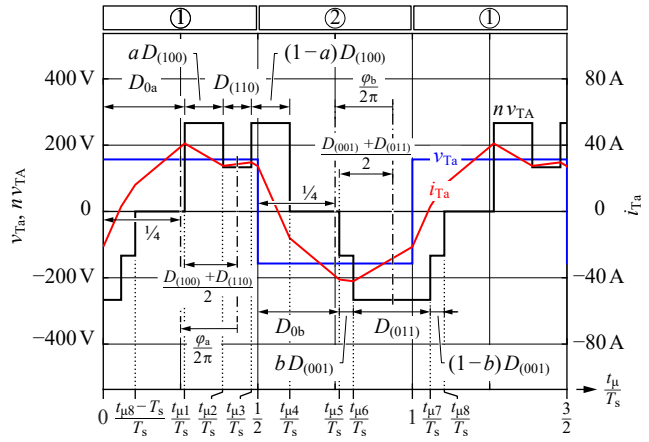

(a)

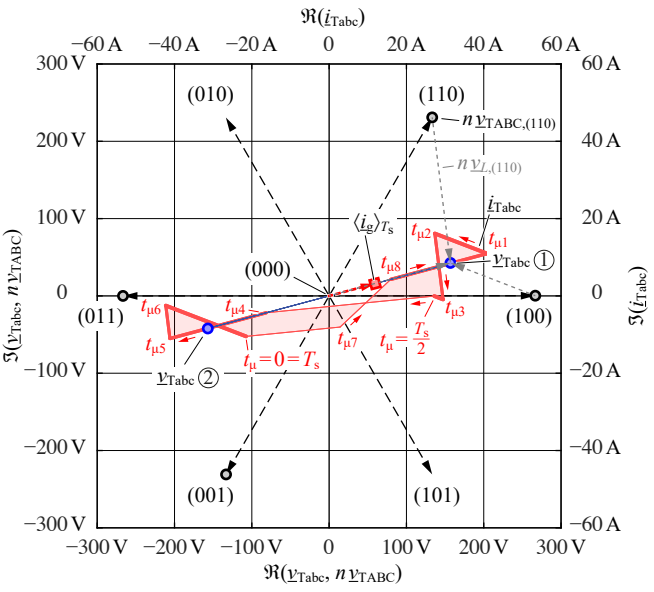

(b)

Fig. 4: (a) Example of waveforms for v_Ta, v_TA, and i_Ta used to define the control parameters φ_a (or D_{0a}), φ_b (or D_{0b}), $D_{(100)}$, $D_{(110)}$, $D_{(001)}$, $D_{(011)}$, a, and b. (b) Example of the trajectory of $\underline{i}_\mathrm{Tabc}$ that results for the operating conditions used in Fig. 4(a). The encircled numbers ① and ② refer to the first and the second half of the switching period, respectively. Furthermore, $\langle \underline{i}_\mathrm{g} \rangle_{T_s}$ refers to the average value of the SV of the grid phase currents i_a, i_b, and i_c over one switching period. For this figure, the settings of Tab. I, $V_\mathrm{dc} = 400\,\mathrm{V}$, and $\phi_\mathrm{g} = 15°$ were considered. Note: the line thickness in Fig. 4(b) is an indicator for the rate at which the trajectory changes (thick line: low rate of change, thin line: high rate of change).

Fig. 4(a) depicts example waveforms of v_Ta, v_TA, and i_Ta that can result for this switching state sequence. According to Fig. 4(a) and under the assumption of a constant (given) switching frequency, eight control parameters can be identified,

$$D_{(100)} = \frac{t_{\mu2} - t_{\mu1} + t_{\mu4} - t_{\mu3}}{T_\mathrm{s}},\quad D_{(110)} = \frac{t_{\mu3} - t_{\mu2}}{T_\mathrm{s}}, \tag{8}$$

$$D_{(001)} = \frac{t_{\mu6} - t_{\mu5} + t_{\mu8} - t_{\mu7}}{T_\mathrm{s}},\quad D_{(011)} = \frac{t_{\mu7} - t_{\mu6}}{T_\mathrm{s}}, \tag{9}$$

$$D_{0a} = \frac{t_{\mu1}}{T_\mathrm{s}},\qquad a = \frac{t_{\mu2} - t_{\mu1}}{D_{(100)} T_\mathrm{s}}, \tag{10}$$

$$D_{0b} = \frac{t_{\mu5}}{T_\mathrm{s}} - \frac{1}{2},\qquad b = \frac{t_{\mu6} - t_{\mu5}}{D_{(001)} T_\mathrm{s}}. \tag{11}$$

In DAB converters, the time displacement of the secondary-side hf ac voltage with respect to the primary-side hf ac voltage (e.g. v_TA versus v_Ta for phase a) is commonly characterized by the phase shifts between the centers of the active time intervals with positive and negative hf ac voltages, φ_a and φ_b. In general, different phase shifts can be present during the first and second half of the switching period,

$$\varphi_\mathrm{a} = 2\pi \left(D_{0a} + \frac{D_{(100)} + D_{(110)}}{2} - \frac{1}{4} \right), \tag{12}$$

$$\varphi_\mathrm{b} = 2\pi \left(D_{0b} + \frac{D_{(001)} + D_{(011)}}{2} - \frac{1}{4} \right). \tag{13}$$

Fig. 4(b) depicts the trajectory of the SV $\underline{i}_\mathrm{Tabc}$ that results for the operating conditions chosen for Fig. 4(a). This trajectory is best explained based on the SV of the inductor voltage, $n\underline{v}_L$, shown in Fig. 2(a). According to Fig. 4(a), the rectifier is in the freewheeling state (000) during $t_{\mu8} - T_\mathrm{s} < t_\mu < t_{\mu1}$. Therefore, $n\underline{v}_L(t_\mu) = \underline{v}_\mathrm{g}$ applies during this time interval and $\underline{i}_\mathrm{Tabc}$ changes along the direction of $\underline{v}_\mathrm{g}$. At $t_\mu = t_{\mu1}$, the rectifier changes its switching state to (001), so $n\underline{v}_L(t_\mu) = \underline{v}_\mathrm{g} - n\underline{v}_{\mathrm{TABC},(100)}$ applies during $t_{\mu1} < t_\mu < t_{\mu2}$. For this reason, $\underline{i}_\mathrm{Tabc}$ changes along a straight line that is parallel to $\underline{v}_\mathrm{g} - n\underline{v}_{\mathrm{TABC},(100)}$. This process then proceeds for all switching states.

In the context of Fig. 4(b), a disadvantage of this graphical SV representation becomes apparent. Due to the missing time information, the peak values can be obtained from the

depicted SV trajectories, but not the rms values. Nevertheless, an optimization of the rms value of the transformer current SV was carried out for this paper. The underlying reason for this is that the copper losses in the transformer windings and the conduction losses of the power semiconductor switches are proportional to the square of the rms value. However, the peak value of the transformer current SV cannot be used to determine its rms value. Consequently, an optimization of the peak value would not be expedient. In order to allow an approximate estimation of the rms value from the depicted SV trajectories, the line width of the trajectory was adapted to the speed at which the trajectory is traversed. A thick line denotes a low rate of change and vice versa. This gives a subjective indication of how long the SV $\underline{i}_{\mathrm{Tabc}}$ remains in a certain area. It is important to emphasize at this point that the rms value of a SV can be calculated exactly, since besides the amplitude and phase information, the time information of the SV is also available for the calculation.

With the modulation scheme of [28], the control parameters $D_{(100)}$, $D_{(110)}$, $D_{(001)}$, $D_{(011)}$ are chosen so that the rectifier forms an average voltage SV equal to $\frac{\underline{v}_{\mathrm{g}}}{2n}$ during $\frac{\varphi_{\mathrm{a}} T_{\mathrm{s}}}{2\pi} \leq t_{\mu} \leq \frac{T_{\mathrm{s}}}{2} + \frac{\varphi_{\mathrm{a}} T_{\mathrm{s}}}{2\pi}$ and $-\frac{\underline{v}_{\mathrm{g}}}{2n}$ during $\frac{T_{\mathrm{s}}}{2} + \frac{\varphi_{\mathrm{b}} T_{\mathrm{s}}}{2\pi} \leq t_{\mu} \leq T_{\mathrm{s}} + \frac{\varphi_{\mathrm{b}} T_{\mathrm{s}}}{2\pi}$. This results in

$$D_{(100)} = D_{(011)} = \frac{\sqrt{3}}{4} M \sin\left(\frac{\pi}{3} - \phi_{\mathrm{g}}\right), \tag{14}$$

$$D_{(110)} = D_{(001)} = \frac{\sqrt{3}}{4} M \sin\left(\phi_{\mathrm{g}}\right), \tag{15}$$

where $M = \frac{\sqrt{2} V_{\mathrm{g}}}{n V_{\mathrm{dc}}} < \frac{2}{\sqrt{3}}$ denotes the modulation index. In addition, equal durations are chosen for the first and second occurrences of the states (100) and (001), and the phase shifts φ_{a} and φ_{b} are set equal,

$$a = b = 0.5, \qquad \varphi_{\mathrm{a}} = \varphi_{\mathrm{b}} = \varphi. \tag{16}$$

Power control is performed by adjusting φ. Rectifier operation of the iYR takes place for $\varphi > 0$, inverter operation for $\varphi < 0$. Maximum power results for $|\varphi| \approx \pi/2$, cf. Fig. 23 in [29].[1] Accordingly, all available control parameters defined in (8) to (11) are used, leaving no degree of freedom (DoF) for optimization.

III. Optimization of the Modulation Scheme

The optimization approach aims to determine the control parameters that minimize the current rms values in the hf ac paths for a given operating point ($\underline{v}_{\mathrm{g}}$, V_{dc}, P), given converter parameters (L, n), and given switching sequence (7). It is assumed that $f_{\mathrm{s}} \gg f_{\mathrm{g}}$ applies, i.e., during a single switching period dc–dc operation is considered. The implemented approach comprises two main methods, which are listed below:

1) A generally applicable method for calculating the rms values of the currents in the hf ac paths of the iYR, which is summarized in **Subsection III-A**.
2) The implemented optimization algorithm, as explained in **Subsections III-B and III-C**. This algorithm comprehensively evaluates the above-mentioned method (calculation of rms values) in order to identify optimal control parameters.

In this and the following sections, the instantaneous apparent power, $\underline{s}$, and rms values in the SV representation are used. Please refer to [38], [39] for a detailed description of these.

A. Calculation of Transformer Currents

In principle, analytical expressions could be derived for calculating the rms values of the transformer currents based on the equivalent circuit depicted in Fig. 2(a). However, depending on the currently present sequence of switching states of both the inverter and the rectifier, i.e. the operating mode of the converter, different expressions result. See **Appendix B** for more details. With the switching state sequence (7), the iYR features more than 50 operating modes.

Consequently, the analytical approach would necessitate the consideration of a large number of case distinctions. Moreover, due to the complexity of the investigated iYR, it is to be expected that either no closed-form expressions for the optimal control parameters can be found or that comparatively extensive expressions result, such as (23) in [40]. In addition, such extensive expressions typically do not provide a deeper insight into the interrelationships of the system than what is possible in the context of numerical optimization. Therefore, in this paper a script-based numerical approach, e.g., implemented in MATLAB, is preferred over the analytical approach.

This script calculates a piecewise linear approximation of the steady-state waveform of $\underline{i}_{\mathrm{Tabc}}(t)$ during a switching period, for given input and output voltages ($\underline{v}_{\mathrm{g}}$, V_{dc}), given converter parameters, given switching sequences, and given control parameters [as defined in (8) to (11)]. In a first step, the instants of all switching operations that occur during a switching period are calculated. The waveforms of the input and output voltages are approximated using piecewise constant functions. Using these waveforms and the equivalent circuit diagram from Fig. 2(a), the steady-state waveform of $\underline{i}_{\mathrm{Tabc}}(t)$ is calculated.

B. Simplifications

From the eight available control parameters, one is required for active power control and one for reactive power control. This leaves six DoFs for optimization. However, it is typically found in the context of a numerical optimization of a control method that the more DoF available, the more difficult it becomes to obtain continuous functions for all control parameters over the entire operating range (ϕ_{g}, V_{dc}, P). Discontinuity points in the functions of the control parameters are usually undesirable, as they can lead to complications in practice. In the experimental system under consideration, for example, the control parameters actually used are precalculated, stored in a table, and finally determined in the microcontroller of the converter by bilinear interpolation. To ensure that the interpolation is not computed across such discontinuities, the operating regions without discontinuities would need to be carefully

[1] Note that the variable δ in [29] is equal to $\varphi/(2\pi)$.

separated from each other. In addition, abrupt changes of the control parameters can excite undesired oscillations in the transformer current in practice.

Therefore, two more simplifications are made. Firstly, equal voltage time areas are assumed during the first and second switching half-periods,

$$D_{(100)} = D_{(011)}, \qquad D_{(110)} = D_{(001)}. \tag{17}$$

This ensures that the average values of the magnetic fluxes in the transformer cores disappear.[2] Furthermore, following the control procedure of [29],

$$\varphi_\mathrm{a} = \varphi_\mathrm{b} = \varphi, \tag{18}$$

is chosen. This leaves three DoFs for the optimization described in the following Section III-C.

The optimization can be accelerated if the range of operating points to be investigated can be reduced. In this context it was mentioned in Section II that in the case of a symmetrical three-phase grid, only one 60° sector of the grid period needs to be studied. A closer examination of the symmetries present with the switching state sequence defined in (7) even reveals that the range for ϕ_g to be examined can be confined to $0 \leq \phi_\mathrm{g} \leq 30°$. In the following, this is explained by an example for $\phi_\mathrm{g} = 10°$ and $\phi_\mathrm{g} = 60° - 10° = 50°$ based on **Fig. 5(a)**. If $\phi_\mathrm{g} = 10°$ applies and the rectifier is in the switching state (100), then the voltage SV $\underline{v}_{L,(100)}|_{\phi_\mathrm{g}=10°} = \underline{v}_\mathrm{g}|_{\phi_\mathrm{g}=10°}/n - \underline{v}_{\mathrm{TABC},(100)}$ is applied to L and the SV $\underline{i}_\mathrm{Tabc}|_{\phi_\mathrm{g}=10°}$ changes along the trajectory marked with ⓘ in Fig. 5(a). For $\phi_\mathrm{g} = 50°$ and if the rectifier is in the switching state (001), the voltage SV $\underline{v}_{L,(001)}|_{\phi_\mathrm{g}=50°} = \underline{v}_\mathrm{g}|_{\phi_\mathrm{g}=50°}/n - \underline{v}_{\mathrm{TABC},(001)}$ is applied to L [marked with ⓘⓘ in Fig. 5(a)]. As is immediately clear from symmetry considerations, $\underline{v}_{L,(100)}|_{\phi_\mathrm{g}=10°}$ and $\underline{v}_{L,(001)}|_{\phi_\mathrm{g}=50°}$ are of equal length and are mirrored about the SV axis (010), i.e., the phase axis of phase B. Based on similar considerations it is found that this also holds true for the inductor voltage SVs of the remaining states and for the average value of the grid current SV over a switching period, $\langle \underline{i}_\mathrm{g} \rangle_{T_\mathrm{s}}$.

If the reactive power requirement over a switching period is zero, i.e., $\Im(\langle \underline{s} \rangle_{T_\mathrm{s}}) = 0$, the values of the control parameters for $30° < \phi_\mathrm{g} < 60°$ that lead to the mirrored trajectory of $\underline{i}_\mathrm{Tabc}$ can be directly determined from the control parameters calculated for $0° < \phi_\mathrm{g} < 30°$ by swapping the control parameters,

$$D_{(001)}|_{\phi_\mathrm{g}=60°-\phi_\mathrm{g0}} = D_{(100)}|_{\phi_\mathrm{g}=\phi_\mathrm{g0}}, \tag{19}$$
$$D_{(011)}|_{\phi_\mathrm{g}=60°-\phi_\mathrm{g0}} = D_{(110)}|_{\phi_\mathrm{g}=\phi_\mathrm{g0}}, \tag{20}$$
$$D_{(100)}|_{\phi_\mathrm{g}=60°-\phi_\mathrm{g0}} = D_{(001)}|_{\phi_\mathrm{g}=\phi_\mathrm{g0}}, \tag{21}$$
$$D_{(110)}|_{\phi_\mathrm{g}=60°-\phi_\mathrm{g0}} = D_{(011)}|_{\phi_\mathrm{g}=\phi_\mathrm{g0}}, \tag{22}$$
$$b|_{\phi_\mathrm{g}=60°-\phi_\mathrm{g0}} = a|_{\phi_\mathrm{g}=\phi_\mathrm{g0}}, \tag{23}$$
$$a|_{\phi_\mathrm{g}=60°-\phi_\mathrm{g0}} = b|_{\phi_\mathrm{g}=\phi_\mathrm{g0}}, \tag{24}$$
$$0° < \phi_\mathrm{g0} < 30°. \tag{25}$$

[2]It should be noted that this only applies to dc operation when there are no load changes. The deviations from dc operation that occur during rectifier/inverter operation or load changes may lead to certain average values of magnetic fluxes and are not investigated in this paper.

Consequently, equal rms values result over a switching period for the original and the mirrored trajectory,

$$\langle \underline{I}_\mathrm{Tabc,rms} \rangle_{T_\mathrm{s}}\big|_{\phi_\mathrm{g}=\phi_\mathrm{g0}} = \langle \underline{I}_\mathrm{Tabc,rms} \rangle_{T_\mathrm{s}}\big|_{\phi_\mathrm{g}=60°-\phi_\mathrm{g0}}. \tag{26}$$

In combination with (17) it follows that for $\phi_\mathrm{g} = 30°$ the

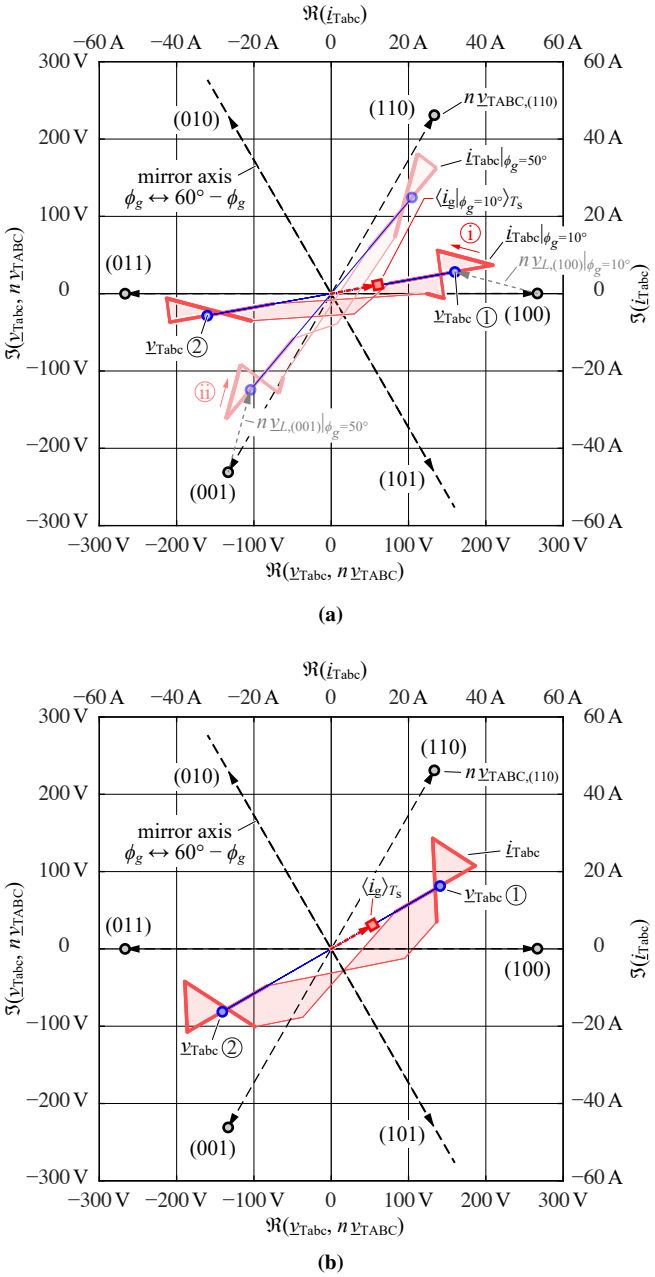

(a)

(b)

Fig. 5: Trajectories of $\underline{i}_\mathrm{Tabc}$ that result during one switching period for the conventional modulation scheme, the settings of Tab. I, and $V_\mathrm{dc} = 400\,\mathrm{V}$: (a) $\phi_\mathrm{g} = 10°$ (ⓘ) and $\phi_\mathrm{g} = 50°$ (ⓘⓘ); (b) $\phi_\mathrm{g} = 30°$. The SV $\langle \underline{i}_\mathrm{g} \rangle_{T_\mathrm{s}}$ refers to the average value of the SV of the grid currents i_a, i_b, and i_c over one switching period.

equalities

$$D_{(100)}|_{\phi_g=30^\circ} = D_{(110)}|_{\phi_g=30^\circ} = \\ = D_{(001)}|_{\phi_g=30^\circ} = D_{(011)}|_{\phi_g=30^\circ}, \quad (27)$$

$$a|_{\phi_g=30^\circ} = b|_{\phi_g=30^\circ} = 0.5 \quad (28)$$

apply. **Fig. 5(b)** shows an example of the trajectory of $\underline{i}_{\mathrm{Tabc}}$ for $\phi_g = 30^\circ$. The mirror symmetry about the phase axis of phase B is clearly visible.

C. Flowchart of the Optimization

The optimization of $\langle \underline{I}_{\mathrm{Tabc,rms}} \rangle_{T_s}$ basically considers the five control parameters φ, $D_{(100)}$, $D_{(110)}$, a, and b that remain after applying the simplifications (17) and (18). Two of these are required to achieve the required active power P and reactive power Q, where in this paper $Q = 0$ is considered so that the rectifier behaves in a purely resistive manner.

For controlling P, the hf phase shift φ can be used [29]. However, in the iYR, φ also slightly affects Q. An example of how P and Q depend on φ is shown in **Fig. 6(a)** for operation with $0 < \varphi < 90^\circ$, $D_{(100)} = 0.277$, $D_{(110)} = 0.066$, $a = 0.504$, $b = 0.481$, $\phi_g = 10^\circ$, $V_{dc} = 400\,\mathrm{V}$, and the remaining settings according to Table I.

The reactive power consumption from the grid, $Q = \Im\{\langle \underline{s} \rangle_{T_s}\}$, can be effectively adjusted by adjusting the ratio

$$c = \frac{D_{(100)}}{D_{(100)} + D_{(110)}} = \frac{D_{(100)}}{D_\Sigma}, \quad (29)$$

since the voltage SVs of the states (100) and (110) point into different directions. Note that changing c also affects P, although less than Q, cf. **Fig. 6(b)**. Thus, the equation set

$$\Re\{\langle \underline{s} \rangle_{T_s}(\varphi, c)\} = P \quad \text{and} \quad \Im\{\langle \underline{s} \rangle_{T_s}(\varphi, c)\} = 0 \quad (30)$$

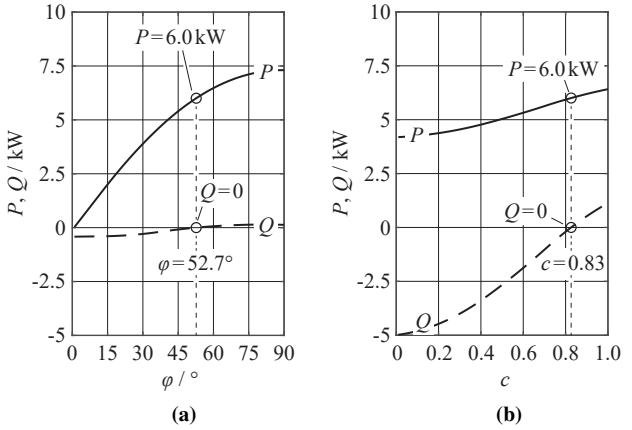

Fig. 6: Characteristics of $P = \Re\{\langle \underline{s} \rangle_{T_s}\}$ and $Q = \Im\{\langle \underline{s} \rangle_{T_s}\}$ as functions of: (a) φ and (b) c for an operating point with $\phi_g = 10^\circ$, $V_{dc} = 400\,\mathrm{V}$, $D_\Sigma = 0.424$, $a = 0.384$, $b = 0.115$ [φ and c are defined in (18) and (29), respectively]. In (a) $c = 0.826$ and in (b) $\varphi = 52.7^\circ$ apply. It can be seen that φ mainly changes P and that c has a strong effect on Q.

must be solved with respect to φ and c in order to achieve the required apparent power over one switching period. Accordingly, D_Σ, a, and b remain for the optimization of the rms value of the transformer current SV. Finally, for known values of D_Σ and c, $D_{(100)}$ and $D_{(110)}$ are calculated with

$$D_{(100)} = c\, D_\Sigma, \qquad D_{(110)} = (1 - c)\, D_\Sigma. \quad (31)$$

The optimization algorithm presented in the following assumes defined converter settings (n, L, f_s) and a defined operating point (V_g, V_{dc}, P). The implemented optimization procedure considers $K = 61$ discrete values of ϕ_g in the range between 0° and 30°,

$$\phi_{g,k} = 30^\circ \frac{k}{K-1} \quad \forall \quad k \in \mathbb{N}_0 \wedge k < K. \quad (32)$$

The actual optimization of the current rms value employs MATLAB's `fmincon` method (configured to use the Sequential Quadratic Programming (SQP) algorithm). Since there is no guarantee that the algorithm finds the global minimum, the result for a local minimum may be returned, which typically leads to unsteady characteristics of the control parameters when examined over the operating range. To avoid this as far as possible, the optimization starts at an initial operating point in which the number of DoFs is reduced. There, the computation of the global minimum is more reliable. According to (27) and (28) this operating point exists for $\phi_g = 30^\circ$, i.e. $k = K - 1$. Thus, only D_Σ remains for the optimization. The value of D_Σ obtained from this optimization is then used to determine the initial values for the less robust subsequent optimization, in which three DoFs are available (a, b, D_Σ). Subsequently, the results of each optimization are used to determine the initial values for the next optimization, which is described later in the context of the explanation of the flow chart shown in Fig. 7(b).

The main flow chart of the optimization procedure is shown in **Fig. 7(a)** to illustrate this process. Note that the circled numbers on the right side of Fig. 7 serve to establish a link to the description given below.

In a first step, the control parameters are optimized for $\phi_g = 30^\circ$ (① in Fig. 7(a)). This is because the start values used for each optimization step are based on the results obtained in the previous optimization step. Since the symmetries at $\phi_g = 30^\circ$ lead to $a = b = 0.5$ (see Subsection III-B), only one parameter (i.e., D_Σ) needs to be optimized at $\phi_g = 30^\circ$. Consequently, the optimization is more robust at this operating point. Subsequently, the control parameters for the remaining grid phase angles $\phi_{g,k} < 30^\circ$ are optimized [steps ②, ③, and ④ in Fig. 7(a)].

For a given grid phase angle, the control parameters are optimized according to the flowchart shown in **Fig. 7(b)**]. In order to make the computation of the global minimum more robust, the optimization is performed for multiple initial values for D_Σ, a, and b. In this context, the list of start values is initialized first, in step ⑤. In total, eleven different start values

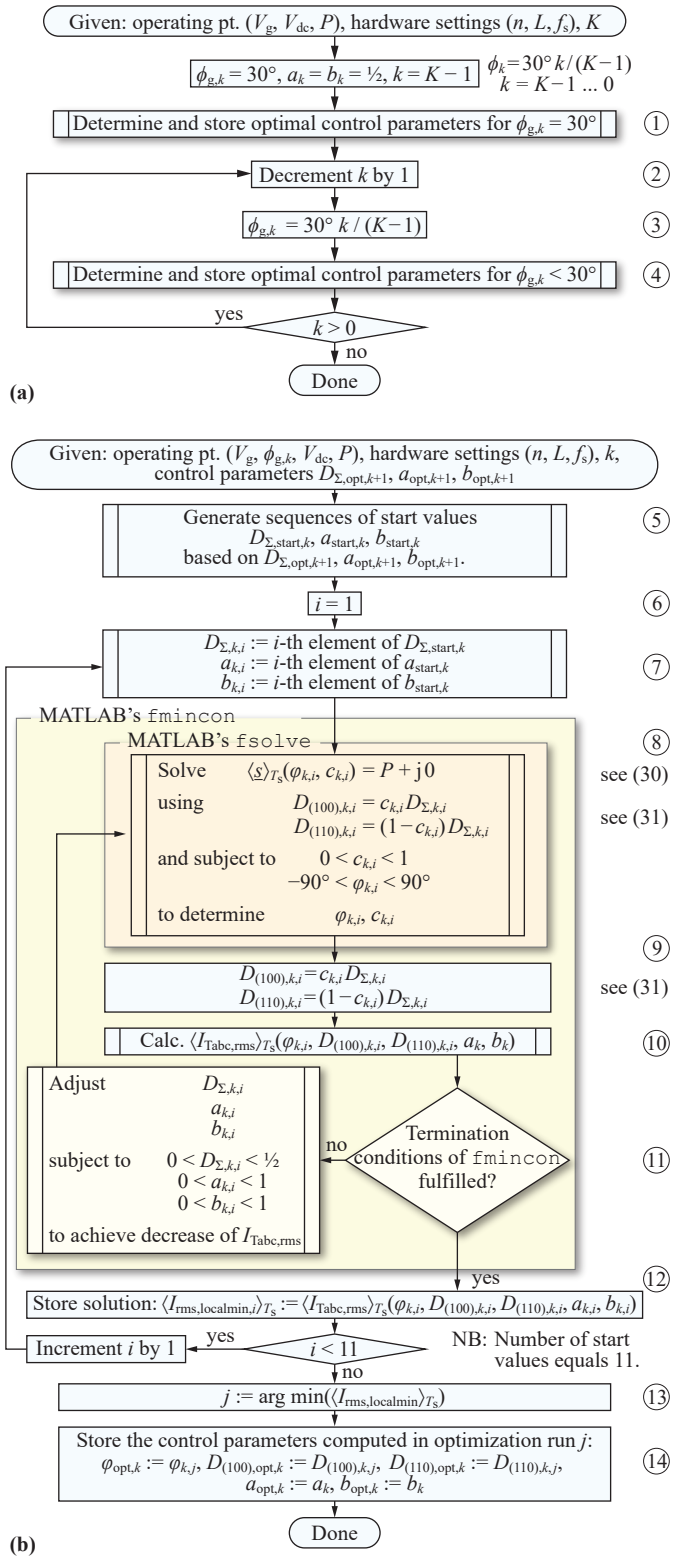

Fig. 7: (a) Main flow chart of the optimization procedure. (b) Flow chart of the subroutine used to determine and store the optimal control parameters.

$D_{\Sigma,k,i}$, $a_{k,i}$, and $b_{k,i}$ are considered, as given in **Table II**.[3] The calculated start values are limited to permissible value ranges according to

$$D_{\Sigma,start,k,i} = \text{clip}(\widetilde{D}_{\Sigma,start,k,i}, 0.01, 0.49), \tag{33}$$

$$a_{start,k,i} = \text{clip}(\widetilde{a}_{start,k,i}, 0.01, 0.99), \tag{34}$$

$$b_{start,k,i} = \text{clip}(\widetilde{b}_{start,k,i}, 0.01, 0.99), \tag{35}$$

$$\text{clip}(x, x_{min}, x_{max}) = \begin{cases} x_{min} & \forall & x < x_{min} \\ x & \forall & x_{min} \le x \le x_{max} \\ x_{max} & \forall & x_{max} < x \end{cases}. \tag{36}$$

In a next step, $D_{\Sigma,k,i}$, $a_{k,i}$, and $b_{k,i}$ are set to the first start values from this list (steps ⑥ and ⑦). Subsequently, MATLAB's `fsolve` method is applied to find the values of $\varphi_{k,i}$ and $c_{k,i}$ such that (30) is fulfilled ⑧.[4] The results for $c_{k,i}$ and $\varphi_{k,i}$ are used to calculate $D_{(100),k,i}$, $D_{(110),k,i}$ ⑨, and $\langle \underline{I}_{Tabc,rms} \rangle_{T_s}$ ⑩. MATLAB's `fmincon` method evaluates the obtained result and adjusts $D_{\Sigma,k,i}$, $a_{k,i}$, and $b_{k,i}$ according to the SQP algorithm or returns the optimization result if the termination conditions are fulfilled ⑪. The obtained solution (rms value of the transformer current SV and related control parameters) of the i-th optimization run is stored in step ⑫ and the optimization for the next initial value is carried out. After all eleven optimization passes have been performed, this algorithm determines the optimization pass that resulted in the lowest value for $I_{Tabc,rms}$ ⑬ and returns the control parameters of this optimization pass ⑭.

Note that the first optimization run for $\phi_g = 30°$ (step ① in Fig. 7(a)) is performed according to a simplified version of the flowchart shown in Fig. 7(b). There, $a = b = 0.5$ and six start values, $D_{\Sigma,start,k} = (0.25, 0.3, 0.35, 0.4, 0.45, 0.49)$, are used.

The complete optimization procedure is performed for $G \times H = 12 \times 21$ different operating points defined by V_{dc} and $I_{dc} = P/V_{dc}$. The range for V_{dc} is divided into $G = 12$ equidistantly distributed values,

$$V_{dc,g} = 200\,\text{V} + \frac{g(750\,\text{V} - 200\,\text{V})}{G-1} \;\forall\; g \in \mathbb{N}_0 \;\wedge\; g < G. \tag{37}$$

With respect to I_{dc}, the maximum dc current that can be achieved for a given value of L, $I_{dc,L,max}$, is determined in a first step. In this context, a detailed inspection of the dc current computed with the numerical method summarized in Subsection III-A reveals two findings. First, it is found that the minimum value of $I_{dc,L,max}$ results for $\phi_g = 30°$. Consequently, the maximum achievable dc current needs to be evaluated for this grid phase angle. Second, $I_{dc,L,max}$ results for $\varphi \approx 90°$ and maximum relative durations $D_{(100)}$ and $D_{(110)}$, which is

[3] The subscript k is added to the control variables, since different optimal control parameters result for different values of k, i.e., for different grid phase angles. For example, the optimal time duration of switching state (100) is referred to with $D_{(100),opt,k}$.

[4] Note that the solver may fail to fulfill (30) for small values of $D_{\Sigma,k,i}$. In this case, the optimization is restarted with the next start value for $D_{\Sigma,k,i}$ [for reasons of keeping a clear presentation, this is not shown in Fig. 7(b)].

not surprising given the DAB-like topology of the iYR. Based on these findings and due to the symmetry conditions (27) and (28), $I_{\mathrm{dc},L,\mathrm{max}}$ can be estimated by evaluating the converter at $\phi_\mathrm{g} = 30°$, $\varphi = 90°$, $D_{(100)} = D_{(110)} = 0.25$, and $a = b = 0.5$. The value determined for $I_{\mathrm{dc},L,\mathrm{max}}$ is divided into $H = 21$ equidistantly distributed values,

$$I_{\mathrm{dc},h} = 90\,\%\, I_{\mathrm{dc},L,\mathrm{max}} \frac{h}{H-1} \;\forall\; h \in \mathbb{N}_0 \;\wedge\; h < H. \tag{38}$$

Note that dc currents up to $90\,\%\, I_{\mathrm{dc},L,\mathrm{max}}$ are considered. This addresses the fact that due to losses and component tolerances in a real system, it may not be possible to achieve $I_\mathrm{dc} = I_{\mathrm{dc},L,\mathrm{max}}$.

In total, the optimization returns $G \times H \times K = 12 \times 21 \times 61 = 15372$ different values for the control parameters. These optimized control parameters are stored in tables that are stored in the microcontroller used to control the converter. The microcontroller determines the control parameters from these table values using bilinear interpolation, cf. [32].

IV. Optimization Results

The improvement achieved by means of optimization is evaluated using the criterion

$$\left(\frac{\langle I_{\mathrm{Tabc,rms,conv}} \rangle_{T_\mathrm{g}}}{\langle I_{\mathrm{Tabc,rms,opt}} \rangle_{T_\mathrm{g}}} \right)^2 - 1. \tag{39}$$

Here, $\langle I_{\mathrm{Tabc,rms,conv}} \rangle_{T_\mathrm{g}}$ and $\langle I_{\mathrm{Tabc,rms,opt}} \rangle_{T_\mathrm{g}}$ denote the average rms values of the transformer current SV for conventional and optimized control, respectively, over a grid period and at a given operating point (except for ϕ_g),

$$\langle I_{\mathrm{Tabc,rms,opt}} \rangle_{T_\mathrm{g}} = \sqrt{\frac{1}{2\pi} \int_0^{2\pi} \left[\langle I_{\mathrm{Tabc,rms,opt}} \rangle_{T_\mathrm{s}}(\phi_\mathrm{g}) \right]^2 \mathrm{d}\phi_\mathrm{g}}\,, \tag{40}$$

$$\langle I_{\mathrm{Tabc,rms,conv}} \rangle_{T_\mathrm{g}} = \sqrt{\frac{1}{2\pi} \int_0^{2\pi} \left[\langle I_{\mathrm{Tabc,rms,conv}} \rangle_{T_\mathrm{s}}(\phi_\mathrm{g}) \right]^2 \mathrm{d}\phi_\mathrm{g}}\,. \tag{41}$$

Accordingly, (39) determines the relative increase in conduction losses at a given operating point.

TABLE II: Definition of how the initial values $\widetilde{D}_{\Sigma,\mathrm{start},k,i}$, $\widetilde{a}_{\mathrm{start},k,i}$, and $\widetilde{b}_{\mathrm{start},k,i}$ used for the optimization for $\phi_{\mathrm{g},k} < 30°$ are calculated from the previous optimization results.

i	$\widetilde{D}_{\Sigma,\mathrm{start},k,i}$	$\widetilde{a}_{\mathrm{start},k,i}$	$\widetilde{b}_{\mathrm{start},k,i}$
1	$D_{\Sigma,\mathrm{opt},k+1}$	$a_{\mathrm{opt},k+1}$	$b_{\mathrm{opt},k+1}$
2	$1.1\, D_{\Sigma,\mathrm{opt},k+1}$	$a_{\mathrm{opt},k+1}$	$b_{\mathrm{opt},k+1}$
3	$0.9\, D_{\Sigma,\mathrm{opt},k+1}$	$a_{\mathrm{opt},k+1}$	$b_{\mathrm{opt},k+1}$
4	$D_{\Sigma,\mathrm{opt},k+1}$	$1.1\, a_{\mathrm{opt},k+1}$	$b_{\mathrm{opt},k+1}$
5	$D_{\Sigma,\mathrm{opt},k+1}$	$0.9\, a_{\mathrm{opt},k+1}$	$b_{\mathrm{opt},k+1}$
6	$D_{\Sigma,\mathrm{opt},k+1}$	$a_{\mathrm{opt},k+1}$	$1.1\, b_{\mathrm{opt},k+1}$
7	$D_{\Sigma,\mathrm{opt},k+1}$	$a_{\mathrm{opt},k+1}$	$0.9\, b_{\mathrm{opt},k+1}$
8	$1.1\, D_{\Sigma,\mathrm{opt},k+1}$	$1.1\, a_{\mathrm{opt},k+1}$	$1.1\, b_{\mathrm{opt},k+1}$
9	$0.9\, D_{\Sigma,\mathrm{opt},k+1}$	$0.9\, a_{\mathrm{opt},k+1}$	$0.9\, b_{\mathrm{opt},k+1}$
10	$1.1\, D_{\Sigma,\mathrm{opt},k+1}$	$0.9\, a_{\mathrm{opt},k+1}$	$0.9\, b_{\mathrm{opt},k+1}$
11	$0.9\, D_{\Sigma,\mathrm{opt},k+1}$	$1.1\, a_{\mathrm{opt},k+1}$	$1.1\, b_{\mathrm{opt},k+1}$

Fig. 8 depicts the values resulting for (39) over the operating range and for the converter settings specified in Table I. Especially in the range of low output currents, $I_\mathrm{dc} < 6\,\mathrm{A}$, the conventional modulation scheme causes significantly higher conduction losses than the optimized modulation scheme. Furthermore, the conventional modulation scheme cannot cover the range with high output voltage and high output currents (e.g., $V_\mathrm{dc} = 750\,\mathrm{V}$ and $I_\mathrm{dc} = 15\,\mathrm{A}$). This is because (14) and (15) determine $D_{(100)}$ and $D_{(110)}$ based on the reciprocal of V_dc without considering I_dc. The resulting reduction in the average voltage SV generated by the rectifier over half a switching period leads to a reduction in the maximum output power.

Fig. 9 depicts the characteristics of $\langle I_{\mathrm{Tabc,rms,opt}} \rangle_{T_\mathrm{s}}(\phi_\mathrm{g})$ and the optimized control parameters for $V_\mathrm{dc} = 200\,\mathrm{V}$ and three different output currents ($I_\mathrm{dc} = 3.14\,\mathrm{A}$, $7.07\,\mathrm{A}$, and $14.1\,\mathrm{A}$) for $0 \le \phi_\mathrm{g} < 60°$. Although the functions of $\langle I_{\mathrm{Tabc,rms,opt}} \rangle_{T_\mathrm{s}}(\phi_\mathrm{g})$ and $\varphi(\phi_\mathrm{g})$ shown in **Fig. 9(a)** and **Fig. 9(b)** are continuous, the functions of $D_{(100)}(\phi_\mathrm{g})$, $D_{(110)}(\phi_\mathrm{g})$, $a(\phi_\mathrm{g})$, and $b(\phi_\mathrm{g})$ shown in **Fig. 9(c)** and **Fig. 9(d)** have discontinuity points, which are undesirable, as mentioned in Subsection III-B.

The reason for such discontinuity points in the control functions is that certain operating points exist at which different values of the control variables lead to the same minimum value of $\langle I_{\mathrm{Tabc,rms}} \rangle_{T_\mathrm{s}}$. In Fig. 9, for example, this is the case for $I_\mathrm{dc} = 14.9\,\mathrm{A}$ and $\phi_\mathrm{g} \approx 17.5°$. However, for $\phi_\mathrm{g} = 17°$ the optimum only occurs for the operating point at $a_\mathrm{III} = 1$ and $b_\mathrm{III} \approx 0.5$, whereas for $\phi_\mathrm{g} = 18°$ the optimum occurs at $a_\mathrm{III} \approx 0.5$ and $b_\mathrm{III} = 0$. Optimization results that lead to control functions with discontinuity points can be found in the literature for other converters, e.g. in [41] in the context of the optimization of the Weighted Total Harmonic Distortion (WTHD) of an inverter, which pursues the aim of minimizing the rms value of the load current. The optimal control functions can also show discontinuity points there, as can be seen in Fig. 9.22 in [41].

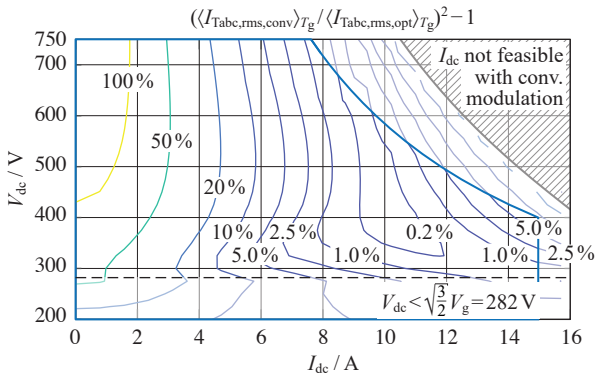

Fig. 8: Results obtained for (39) over the operating range (indicated by the blue line) and for the converter settings (f_s, n, L) specified in Table I. The optimized modulation scheme achieves lower conduction losses, especially in the low power range. Note that the conventional modulation scheme cannot cover the range of high output voltages and output currents (hatched area).

V. Simplified Modulation Scheme

According to Fig. 9, especially the functions of a and b show pronounced discontinuities. To avoid these, it is reasonable to determine the rms values of the transformer currents that can be achieved for constant values for a and b. With $a = b = 0.5$, the conventional modulation scheme achieves a rms value of the transformer current that is close to the optimized value over a relatively wide operating range, cf. Fig. 8 for $I_{\mathrm{dc}} > 7\,\mathrm{A}$. For this reason, a suboptimal modulation scheme with $a = b = 0.5$ is investigated. The underlying idea is that this leaves only D_Σ as a DoF for optimization, which supports the generation of continuous functions for $D_{(100)}$ and $D_{(110)}$. The optimization of the control parameters for the suboptimal modulation scheme is carried out according to Fig. 7 with the only difference that $a = b = 0.5$ is considered for all values of ϕ_{g}, i.e. for $0 \le k \le K-1$.

Fig. 10(a) and **Fig. 10(b)** depict the results for

$$\left(\frac{\langle I_{\mathrm{Tabc,rms,subopt}}\rangle_{T_{\mathrm{g}}}}{\langle I_{\mathrm{Tabc,rms,opt}}\rangle_{T_{\mathrm{g}}}}\right)^2 - 1, \tag{42}$$

$$\left(\frac{\langle I_{\mathrm{Tabc,rms,conv}}\rangle_{T_{\mathrm{g}}}}{\langle I_{\mathrm{Tabc,rms,subopt}}\rangle_{T_{\mathrm{g}}}}\right)^2 - 1. \tag{43}$$

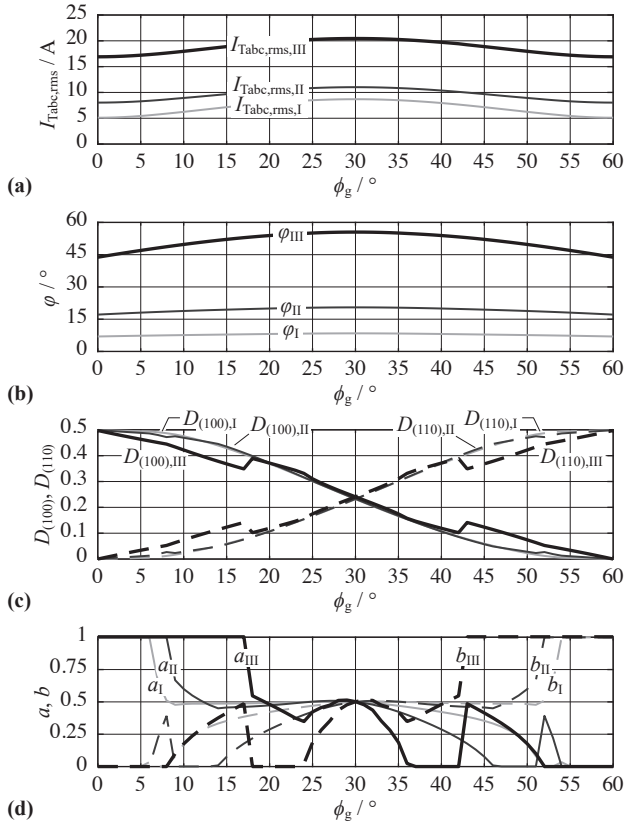

Fig. 9: (a) Characteristics of $\langle I_{\mathrm{Tabc,rms,opt}}\rangle_{T_{\mathrm{s}}}$ for $V_{\mathrm{dc}} = 200\,\mathrm{V}$ and three different output currents (I: $I_{\mathrm{dc}} = 3.14\,\mathrm{A}$, II: $I_{\mathrm{dc}} = 7.07\,\mathrm{A}$, III: $I_{\mathrm{dc}} = 14.9\,\mathrm{A}$) for $0° \le \phi_{\mathrm{g}} \le 60°$. (b)–(d) Characteristics of the optimized control parameters that lead to $\langle I_{\mathrm{Tabc,rms,opt}}\rangle_{T_{\mathrm{g}}}$ depicted in subfigure (a). The plots shown in subfigures (c) and (d) reveal clearly noticeable discontinuity points.

There, $\langle I_{\mathrm{Tabc,rms,subopt}}\rangle_{T_{\mathrm{g}}}$ denotes the overall rms value of $\langle I_{\mathrm{Tabc,rms,subopt}}\rangle_{T_{\mathrm{s}}}$ over a grid period,

$$\langle I_{\mathrm{Tabc,rms,subopt}}\rangle_{T_{\mathrm{g}}} = \sqrt{\frac{1}{2\pi}\int_0^{2\pi} \left[\langle I_{\mathrm{Tabc,rms,subopt}}\rangle_{T_{\mathrm{s}}}(\phi_{\mathrm{g}})\right]^2 \mathrm{d}\phi_{\mathrm{g}}}\,. \tag{44}$$

According to Fig. 10(a), $\langle I_{\mathrm{Tabc,rms,subopt}}\rangle_{T_{\mathrm{g}}} \approx \langle I_{\mathrm{Tabc,rms,opt}}\rangle_{T_{\mathrm{g}}}$ is achieved for most operating points. Only operation with low output voltage and low output current results in a significant value of (42) (e.g. of approximately $10\,\%$ at $V_{\mathrm{dc}} = 200\,\mathrm{V}$ and $I_{\mathrm{dc}} = 5\,\mathrm{A}$).

According to Fig. 10(b), the suboptimal modulation scheme achieves a significant reduction in the transformer rms current values, particularly in the range of high V_{dc} and low I_{dc}. This relationship is also apparent from the SV trajectories shown in **Fig. 11(a)** for $V_{\mathrm{dc}} = 750\,\mathrm{V}$, $P = 1.2\,\mathrm{kW}$, and $\phi_{\mathrm{g}} = 10°$. There, $\langle I_{\mathrm{Tabc,rms,conv}}\rangle_{T_{\mathrm{s}}}$ and $\langle I_{\mathrm{Tabc,rms,subopt}}\rangle_{T_{\mathrm{s}}}$ equal

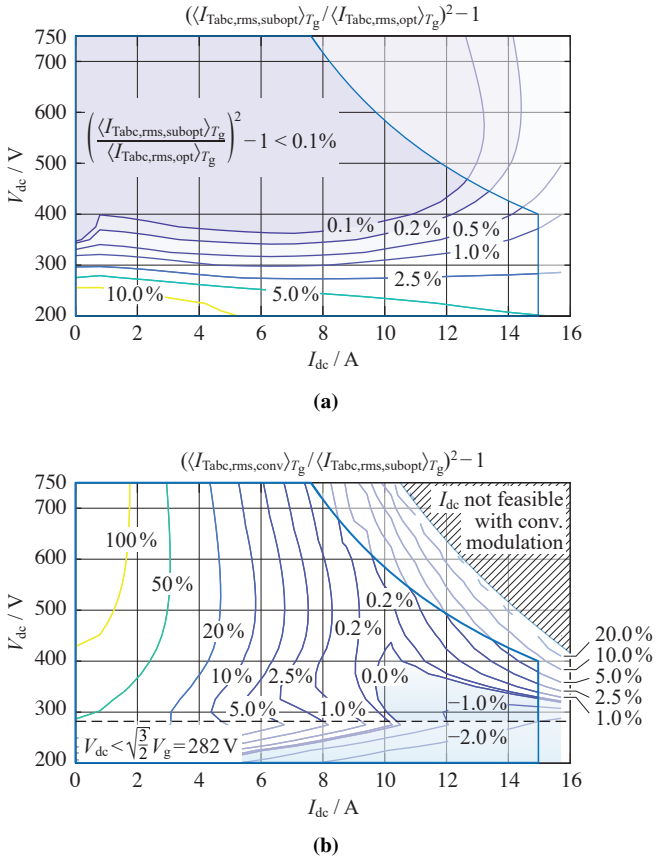

Fig. 10: (a) Results obtained for (42) over the operating range (indicated by the blue line) and for the converter settings (f_{s}, n, L) specified in Table I. According to this result, the rms values of the transformer currents optimized for $a = b = 0.5$ are close to the comprehensively optimized values at most operating points. (b) Results obtained for (43), calculated for the same conditions as for subfigure (a). Interestingly, for $I_{\mathrm{dc}} > 6\,\mathrm{A}$ and $V_{\mathrm{dc}} < 350\,\mathrm{V}$ an operating range is observed (shaded blue), where the control parameters of the suboptimal modulation scheme lead to slightly higher conduction losses than those of the conventional modulation scheme. This is caused by the constraint $Q = 0$ considered for the optimization, as explained in the text.

to 16.0 A and 11.1 A result for the two modulation schemes. This figure reveals that the maximum magnitudes of the SVs are substantially larger for the conventional modulation scheme than for the suboptimal modulation scheme. For completeness, **Fig. 11(b)** shows the waveforms of i_{Ta} for the same operating point and over two switching periods. This figure clearly reveals that the suboptimal modulation scheme achieves a lower rms value of the transformer current SV than the conventional modulation.

A further interesting result of Fig. 10(b) is the blue shaded range at $I_{\mathrm{dc}} > 6\,\mathrm{A}$ and $V_{\mathrm{dc}} < 350\,\mathrm{V}$. In this marked range, $\langle I_{\mathrm{Tabc,rms,subopt}}\rangle_{T_{\mathrm{g}}} > \langle I_{\mathrm{Tabc,rms,conv}}\rangle_{T_{\mathrm{g}}}$ applies, which seems to challenge the validity of the optimization. This result can be attributed to two reasons. First, the conventional modulation scheme keeps φ constant, where the value for φ is selected in such a way that the iYR provides the required power on average over a grid period. However, for constant φ, a fluctuation of the instantaneous power can result, as shown in **Fig. 12(a)** for an example operating point ($V_{\mathrm{dc}} = 200\,\mathrm{V}$, $P = 3\,\mathrm{kW}$). This is not the case for the suboptimal modulation scheme, where the control parameters are continuously adjusted to result in a constant instantaneous power. According to **Fig. 12(b)**, this leads to larger changes in $\langle I_{\mathrm{Tabc,rms,subopt}}\rangle_{T_s}$ over ϕ_{g} (gray curve) than for $\langle I_{\mathrm{Tabc,rms,conv}}\rangle_{T_s}$. Consequently, a slightly larger total rms value results for the suboptimal modulation scheme. If, instead, the control parameters for the suboptimal modulation scheme are determined on the basis of the function of the instantaneous power that results for conventional modulation, i.e., for the red curve in Fig. 12(a), the bold black function is obtained for $\langle I_{\mathrm{Tabc,rms,subopt}}\rangle_{T_s}$. Interestingly, it is immediately apparent that this curve still results in a higher average rms value than that of the conventional modulation scheme.

This leads to the second reason, namely that the boundary condition $Q = 0$ is not considered in the conventional scheme. By removing this constraint from the optimization, a further reduction in the current rms value can be obtained. This result is rather unexpected, i.e., for a given average power and non-zero average reactive power over a switching period, the rms value of the transformer current can be reduced. **Fig. 13** illustrates this relationship for $V_{\mathrm{dc}} = 200\,\mathrm{V}$, $\langle p_{\mathrm{subopt}}\rangle_{T_{\mathrm{s}}} = 3.04\,\mathrm{kW}$, and $\phi_{\mathrm{g}} = 10°$. There, the conventional modulation scheme causes a reactive power of $107\,\mathrm{VA_r}$ and $\langle I_{\mathrm{Tabc,rms,conv}}\rangle_{T_{\mathrm{s}}} = 18.96\,\mathrm{A}$. The optimized scheme achieves $\langle I_{\mathrm{Tabc,rms,opt}}\rangle_{T_{\mathrm{s}}} = 19.3\,\mathrm{A}$ for $\langle q\rangle_{T_{\mathrm{s}}} = 0$, which decreases with increasing reactive power. For $\langle q\rangle_{T_{\mathrm{s}}} = 107\,\mathrm{VA_r}$, $\langle I_{\mathrm{Tabc,rms,opt}}\rangle_{T_{\mathrm{s}}} = 18.95\,\mathrm{A} < \langle I_{\mathrm{Tabc,rms,conv}}\rangle_{T_{\mathrm{s}}}$ results.

This unexpected result can be explained by the working principle of the primary-side part of the iYR which comprises

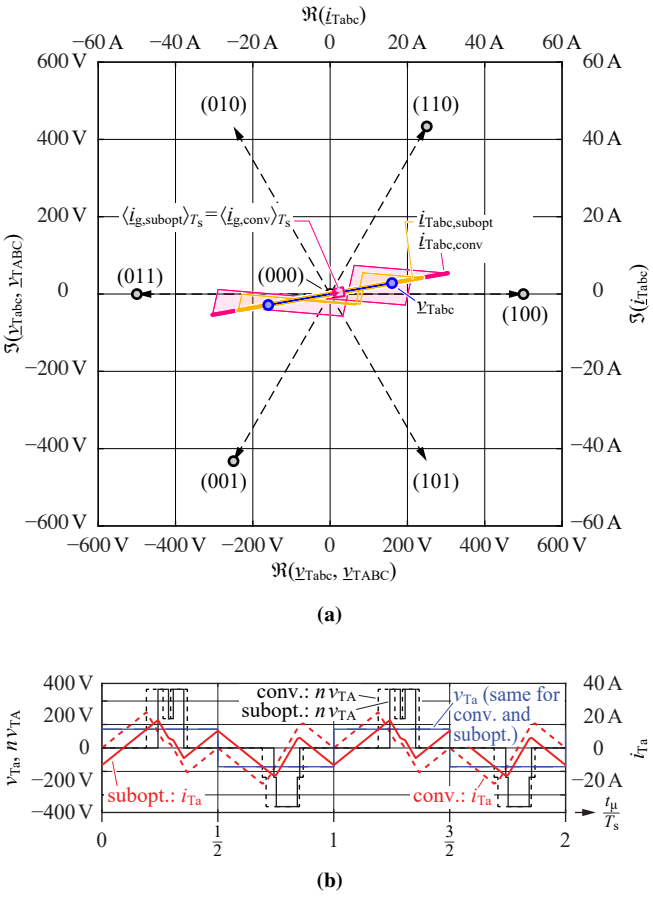

Fig. 11: (a) SV trajectories of $\underline{i}_{\mathrm{Tabc}}$ for the conventional (yellow) and the suboptimal (magenta) modulation schemes: $\langle I_{\mathrm{Tabc,rms,conv}}\rangle_{T_{\mathrm{s}}} = 16.0\,\mathrm{A}$, $\langle I_{\mathrm{Tabc,rms,subopt}}\rangle_{T_{\mathrm{s}}} = 11.1\,\mathrm{A}$. (b) Waveforms of i_{Ta} for suboptimal (solid lines) and conventional (dashed lines) modulation. Operating point: $V_{\mathrm{dc}} = 750\,\mathrm{V}$, $P = 1.2\,\mathrm{kW}$, and $\phi_{\mathrm{g}} = 10°$.

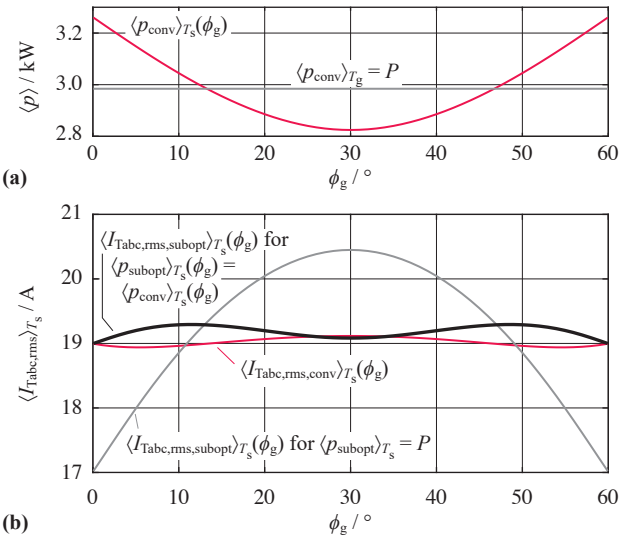

Fig. 12: (a) Characteristic of $\langle p_{\mathrm{conv}}\rangle_{T_{\mathrm{s}}}$ as function of ϕ_{g}, which results for the conventional modulation for $V_{\mathrm{dc}} = 200\,\mathrm{V}$ and $\varphi = 50.7°$. (b) Characteristics of $\langle I_{\mathrm{Tabc,rms,conv}}\rangle_{T_{\mathrm{s}}}$ and $\langle I_{\mathrm{Tabc,rms,subopt}}\rangle_{T_{\mathrm{s}}}$ as functions of ϕ_{g}. $\langle I_{\mathrm{Tabc,rms,subopt}}\rangle_{T_{\mathrm{s}}}$ is once determined for constant power (gray curve) and once for $\langle p_{\mathrm{conv}}\rangle_{T_{\mathrm{s}}}$ (solid black curve). The rms values of the currents over a grid period are: $\langle I_{\mathrm{Tabc,rms,conv}}\rangle_{T_{\mathrm{g}}} = 19.0\,\mathrm{A}$ (magenta curve), $\langle I_{\mathrm{Tabc,rms,subopt}}\rangle_{T_{\mathrm{g}}} = 19.3\,\mathrm{A}$ if $\langle p_{\mathrm{subopt}}\rangle_{T_{\mathrm{s}}}$ is kept constant (gray curve), and $\langle I_{\mathrm{Tabc,rms,subopt}}\rangle_{T_{\mathrm{g}}} = 19.2\,\mathrm{A}$ if $\langle p_{\mathrm{subopt}}\rangle_{T_{\mathrm{s}}}(\phi_{\mathrm{g}}) = \langle p_{\mathrm{conv}}\rangle_{T_{\mathrm{s}}}(\phi_{\mathrm{g}})$ applies (black curve).

the line filter and the primary-side switching stage of the iYR. The primary-side switching stage of the iYR forms the time characteristic of the unfiltered grid current SV by transferring $\underline{i}_{\mathrm{Tabc}}$ to the grid side during half the switching period. The line filter (symbolized by the filter capacitors on the grid side in Fig. 1(a)) suppresses the HF components of this highly fluctuating unfiltered grid current SV. In most cases, the hf ac trajectory of the transformer current SV and the grid voltage SV have different directions. Consequently, a certain phase shift between the grid current SV and the grid voltage SV can enable the trajectory of the transformer SV to be shaped in such a way that a lower rms value $\langle I_{\mathrm{Tabc,rms}}\rangle_{T_\mathrm{s}}$ results. As a result, the dependence of $\langle I_{\mathrm{Tabc,rms,subopt}}\rangle_{T_\mathrm{s}}$ on $\langle q\rangle_{T_\mathrm{s}}$ is a function of ϕ_g. For $\phi_\mathrm{g} = 30°$, the minimum value of $\langle I_{\mathrm{Tabc,rms,subopt}}\rangle_{T_\mathrm{s}}$ is achieved for $\langle q\rangle_{T_\mathrm{s}} = 0$. For $\phi_\mathrm{g} = 50°$, the function shown in Fig. 13 mirrored about the y-axis results for $\langle I_{\mathrm{Tabc,rms,subopt}}\rangle_{T_\mathrm{s}}$, i.e., in this case a reduction of $\langle I_{\mathrm{Tabc,rms,subopt}}\rangle_{T_\mathrm{s}}$ can be achieved for $\langle q\rangle_{T_\mathrm{s}} < 0$.

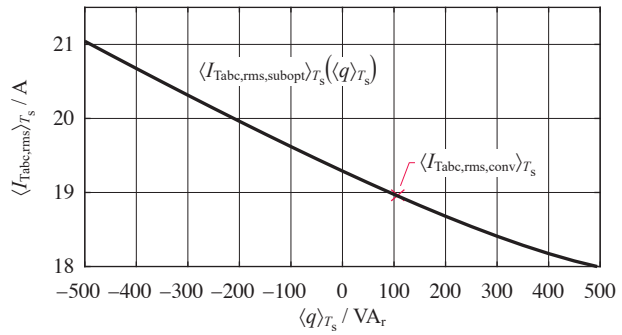

Fig. 13: Dependence of $\langle I_{\mathrm{Tabc,rms,subopt}}\rangle_{T_\mathrm{s}}$ on $\langle q\rangle_{T_\mathrm{s}}$ for $V_\mathrm{dc} = 200\,\mathrm{V}$, $\langle p_{\mathrm{subopt}}\rangle_{T_\mathrm{s}} = 3.04\,\mathrm{kW}$, and $\phi_\mathrm{g} = 10°$. At this operating point, the conventional modulation scheme generates $\langle q\rangle_{T_\mathrm{s}} = 107\,\mathrm{VA_r}$ and $\langle I_{\mathrm{Tabc,rms,conv}}\rangle_{T_\mathrm{s}} = 18.96\,\mathrm{A}$. For the same reactive power, the suboptimal modulation scheme yields $\langle I_{\mathrm{Tabc,rms,subopt}}\rangle_{T_\mathrm{s}} = 18.95\,\mathrm{A}$.

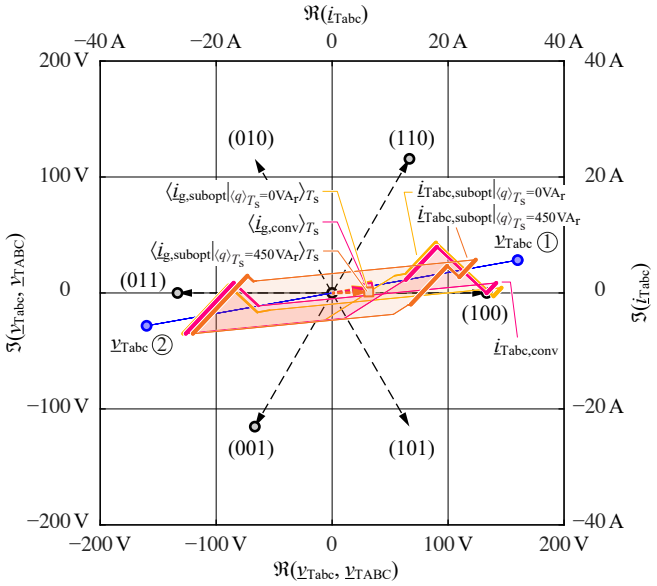

Fig. 14: SV trajectories of $\underline{i}_{\mathrm{Tabc}}$ for the suboptimal modulation scheme using $\langle q\rangle_{T_\mathrm{s}} = 0$ (yellow) and $\langle q\rangle_{T_\mathrm{s}} = 450\,\mathrm{VA_r}$ (orange) and the conventional modulation scheme (magenta). The encircled numbers ① and ② refer to the first and the second half of the switching period, respectively, and $\langle \underline{i}_\mathrm{g}\rangle_{T_\mathrm{s}}$ refers to the average value of the SV formed by i_a, i_b, and i_c over one switching period. Operating point: $V_\mathrm{dc} = 200\,\mathrm{V}$, $\langle p_{\mathrm{subopt}}\rangle_{T_\mathrm{s}} = 3.04\,\mathrm{kW}$, and $\phi_\mathrm{g} = 10°$.

In the following, this remarkable characteristic of the iYR is examined in more detail. **Fig. 14** depicts the trajectories of $\underline{i}_{\mathrm{Tabc}}$ that result for the same operating point ($V_\mathrm{dc} = 200\,\mathrm{V}$, $\langle p_{\mathrm{subopt}}\rangle_{T_\mathrm{s}} = 3.04\,\mathrm{kW}$, and $\phi_\mathrm{g} = 10°$), for the conventional modulation scheme and for the suboptimal modulation scheme using $\langle q\rangle_{T_\mathrm{s}} = 0$ and $\langle q\rangle_{T_\mathrm{s}} = 450\,\mathrm{VA_r}$. This figure shows that the maximum distance of the trajectory of $\underline{i}_{\mathrm{Tabc}}$ from the origin is slightly less for the conventional scheme than for the suboptimal modulation scheme at $\langle q\rangle_{T_\mathrm{s}} = 0$. However, the reduction in the distance of the trajectory from the origin becomes particularly apparent for the suboptimal modulation scheme at $\langle q\rangle_{T_\mathrm{s}} = 450\,\mathrm{VA_r}$. Nevertheless, this finding does not yet provide a relationship to the rms value of a trajectory of the SV, $\langle I_{\mathrm{Tabc,rms,conv}}\rangle_{T_\mathrm{s}}$, as not only the value of the SV, but also the duration for which the SV remains at a certain value determines its rms value. It is therefore important to know not only the value of the SV but also the speed of the SV, which is indicated by the line thickness in Fig. 14. A thick line indicates a low speed. According to Fig. 14, the SV $\underline{i}_{\mathrm{Tabc}}(t)$ stays in the outer areas of the trajectories for relatively long times in all three cases shown, which means that the rms value is highest for suboptimal modulation with $\langle q\rangle_{T_\mathrm{s}} = 0$ ($\langle I_{\mathrm{Tabc,rms,subopt},\langle q\rangle_{T_\mathrm{s}}=0}\rangle_{T_\mathrm{s}} = 19.3\,\mathrm{A}$), in between for conventional modulation ($\langle I_{\mathrm{Tabc,rms,conv}}\rangle_{T_\mathrm{s}} = 19.0\,\mathrm{A}$), and lowest for suboptimal modulation with $\langle q\rangle_{T_\mathrm{s}} = 450\,\mathrm{VA_r}$ ($\langle I_{\mathrm{Tabc,rms,subopt},\langle q\rangle_{T_\mathrm{s}}=450\,\mathrm{VA_r}}\rangle_{T_\mathrm{s}} = 18.1\,\mathrm{A}$).

Fig. 15 depicts the characteristics of $\langle I_{\mathrm{Tabc,rms,subopt}}\rangle_{T_\mathrm{s}}(\phi_\mathrm{g})$ and the optimized control parameters for $V_\mathrm{dc} = 200\,\mathrm{V}$ and three different output currents ($I_\mathrm{dc} = 3.14\,\mathrm{A}$, $7.07\,\mathrm{A}$, and $14.9\,\mathrm{A}$ for $0 \le \phi_\mathrm{g} < 60°$), which are now continuous. Overall, a comprehensive evaluation in the considered operating range reveals that continuous characteristics result for all control parameters for the suboptimal modulation scheme.

Fig. 16, **Fig. 17**, and **Fig. 18** present $\langle I_{\mathrm{Tabc,rms,subopt}}\rangle_{T_\mathrm{s}}$ and the associated control parameters as functions of P, ϕ_g, and V_dc, respectively. For comparison, these figures also include $\langle I_{\mathrm{Tabc,rms,conv}}\rangle_{T_\mathrm{s}}$ and the associated control parameters determined with the conventional modulation scheme. For the respective constant values, $V_\mathrm{dc} = 400\,\mathrm{V}$, $\phi_\mathrm{g} = 10°$, and $P = 3\,\mathrm{kW}$ were selected.

Fig. 16 shows an increase of the optimized values for $D_{(100)}$ and $D_{(110)}$ with increasing power. Accordingly, the increased rms values of the transformer currents that result for the conventional modulation scheme at low and very high power levels can be explained by the fact that in (14) and (15) the control parameters $D_{(100)}$ and $D_{(110)}$ are independent of P. However, it can be seen from Fig. 17 and Fig. 18 that their dependencies on ϕ_g and V_dc as set by (14) and (15) are close to those obtained by the optimization. According to Fig. 16

and Fig. 18, substantial improvements can be achieved in low power and high output voltage ranges. By way of example, the rms value can be decreased from 19.6 A to 17.6 A for $V_{\mathrm{dc}} = 750\,\mathrm{V}$, $\phi_{\mathrm{g}} = 10°$, and $P = 3\,\mathrm{kW}$.

VI. Experimental Results

The experimental verification has been carried out over a full grid period and for following three operating conditions (OC):

- OC1: $V_{\mathrm{dc}} = 400\,\mathrm{V}$, $P = 20\,\%P_{\mathrm{nom}} = 1.2\,\mathrm{kW}$.
- OC2: $V_{\mathrm{dc}} = 400\,\mathrm{V}$, $P = 35\,\%P_{\mathrm{nom}} = 2.1\,\mathrm{kW}$.
- OC3: $V_{\mathrm{dc}} = 400\,\mathrm{V}$, $P = 75\,\%P_{\mathrm{nom}} = 4.5\,\mathrm{kW}$.

The first two operating conditions were selected because the suboptimal modulation scheme achieves a significant improvement of the rms value there, as shown in Fig. 10(b). The third operating condition is used for verification of the operation in the power range with more than 50 % of the nominal load.

The hardware demonstrator employed for this verification realizes the topology depicted in Fig. 1(a) and features the general parameters listed in Tab. I. It has to be pointed out that this hardware demonstrator is only used for the purpose of verifying the presented modulation scheme. Since the optimization objective is to achieve a low rms value of the SV of the grid current over a grid period, this Section focuses on the verification of this rms value. Consequently, it must be ensured that parasitic effects cause only minor deviations of the rms values. In particular, a high accuracy of the pulse waveforms at the switching nodes concerning timing and voltage levels is important. Furthermore, the value of the total inductance L must accurately match the required value. Accurate pulse

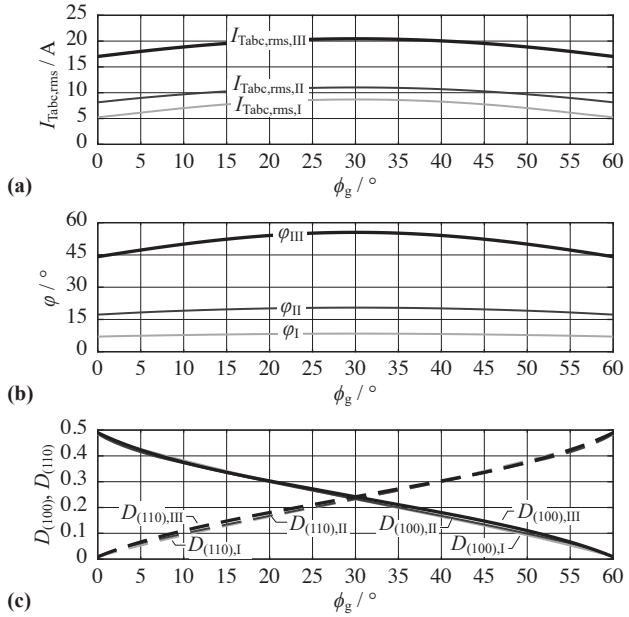

Fig. 15: (a) Characteristics of $\langle I_{\mathrm{Tabc,rms,subopt}}\rangle_{T_{\mathrm{s}}}$ for $V_{\mathrm{dc}} = 200\,\mathrm{V}$ and three different output currents (I: $I_{\mathrm{dc}} = 3.14\,\mathrm{A}$, II: $I_{\mathrm{dc}} = 7.07\,\mathrm{A}$, III: $I_{\mathrm{dc}} = 14.9\,\mathrm{A}$) for $0° \leq \phi_{\mathrm{g}} \leq 60°$. (b)–(c) Characteristics of the optimized control parameters that lead to $\langle I_{\mathrm{Tabc,rms,opt}}\rangle_{T_{\mathrm{g}}}$ depicted in subfigure (a). Note that $a = b = 0.5$ applies for the suboptimal modulation scheme. Compared to Fig. 9, the plots reveal no discontinuity points.

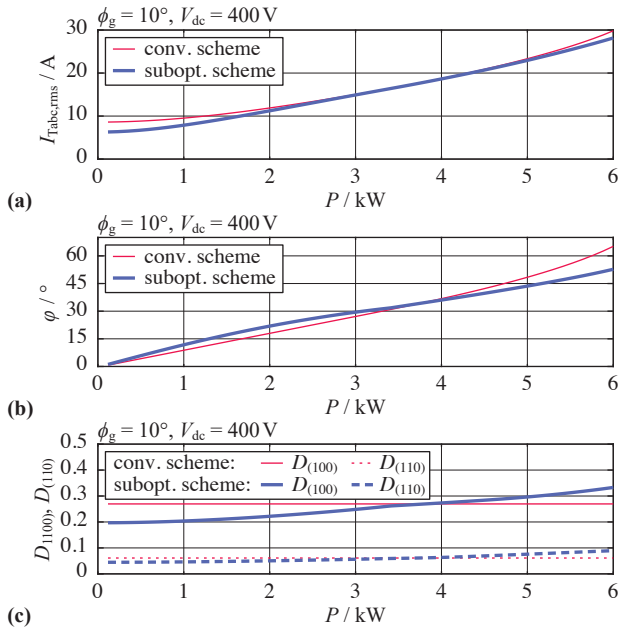

Fig. 16: (a) Characteristics of $\langle I_{\mathrm{Tabc,rms,subopt}}\rangle_{T_{\mathrm{s}}}$ for $\phi_{\mathrm{g}} = 10°$, $V_{\mathrm{dc}} = 400\,\mathrm{V}$, and $0 \leq P \leq 6\,\mathrm{kW}$; n and L as given in Table I. (b) and (c) Characteristics of the control parameters of the suboptimal modulation scheme that lead to $\langle I_{\mathrm{Tabc,rms,subopt}}\rangle_{T_{\mathrm{s}}}$ depicted in subfigure (a).

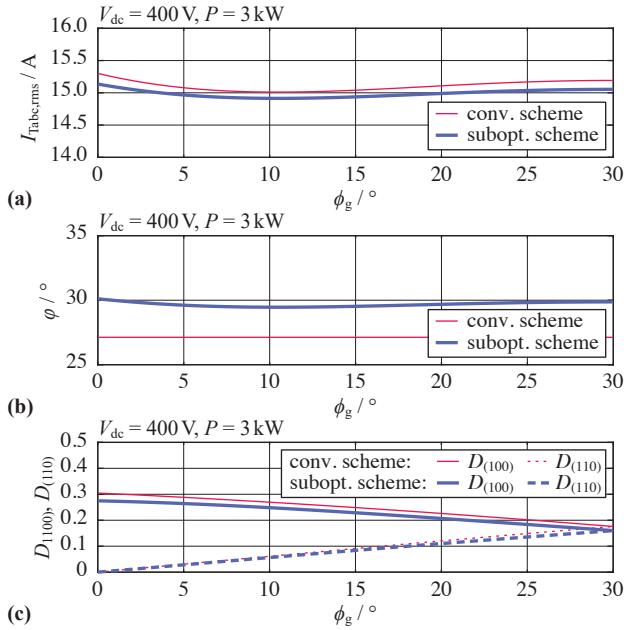

Fig. 17: (a) Characteristics of $\langle I_{\mathrm{Tabc,rms,subopt}}\rangle_{T_{\mathrm{s}}}$ for $0° \leq \phi_{\mathrm{g}} \leq 30°$, $V_{\mathrm{dc}} = 400\,\mathrm{V}$, and $P = 3\,\mathrm{kW}$; n and L as given in Table I. (b) and (c) Characteristics of the control parameters of the suboptimal modulation scheme that lead to $\langle I_{\mathrm{Tabc,rms,subopt}}\rangle_{T_{\mathrm{s}}}$ depicted in subfigure (a).

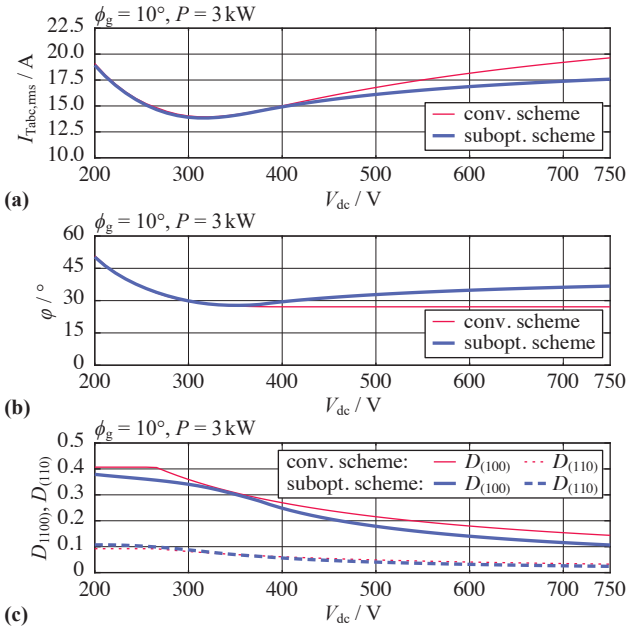

Fig. 18: (a) Characteristics of $\langle I_{\mathrm{Tabc,rms,subopt}} \rangle_{T_s}$ for $\phi_g = 10°$, $200\,V \leq V_{dc} \leq 750\,V$, and $P = 3\,kW$; n and L as given in Table I. (b) and (c) Characteristics of the control parameters of the suboptimal modulation scheme that lead to $\langle I_{\mathrm{Tabc,rms,subopt}} \rangle_{T_s}$ depicted in subfigure (a).

waveforms are achieved by using fast SiC MOSFETs with low on-state resistances (Cree C3M0016120K, one device per switch) and fast gate drivers (Infineon 1ED3124MU12F). This allows to set the dead time, i.e., the time between the turn-off and turn-on processes of the MOSFETs of a half bridge, to a low value of $140\,ns$ (corresponding to $1\,\%$ of T_s). With regard to the three transformers, power components that are readily available in our laboratory have been used. Each transformer has primary and secondary self-inductances of $L_1 = L_2 = 620\,\mu H$, a leakage inductance of $L_\sigma = 7.3\,\mu H$, and a turns ratio of one. Carefully adjusted external inductors (inductance of $6.7\,\mu H$ each) have been connected in series to these transformers on the secondary side, resulting in a total inductance of $14\,\mu H$ in each phase.[5] With regard to the capacitors, three grid-side filter capacitors [e.g. C_a in Fig. 1(a)] with $4\,\mu F$ each (WIMA MKP4 film capacitors), three primary-side series capacitors [e.g. C_s in Fig. 1(a)] with $4.7\,\mu F$ each (WIMA MKP10 film capacitors) and an output-side capacitor $C_{dc} = 360\,\mu F$ (consisting of $6 \times 60\,\mu F$ polypropylene film capacitors by TDK) have been used. A Xilinx Zynq-7000 system-on-chip component, which is operated with a digital clock frequency of $100\,MHz$, realizes the digital control.

Both the conventional and the suboptimal modulation scheme operate the iYR in such a way that a transfer of a defined amount of energy, e.g. from the grid side to the dc side, is achieved during one switching period. Consequently, the iYR can achieve approximately sinusoidal grid currents also without a closed-loop control of the three phase currents. However, the modulator must know the currently present grid phase angle so that the correct gate signals can be generated. In this setup, this detection of the phase angle is done by means of a digital phase-locked loop.

Fig. 19 presents different measured voltage and current waveforms over 2.5 grid periods ($= 50\,ms$). **Fig. 19(a)** and **Fig. 19(b)** show results for operation with suboptimal modulation for OC1. Fig. 19(a) shows the phase-to-neutral voltage of grid phase a and the three grid currents. This measurement illustrates the correct three-phase operation of the demonstrator. The total harmonic distortions (THD) of the grid phase currents i_a, i_b, and i_c are $2.26\,\%$, $2.22\,\%$, and $2.21\,\%$, respectively. As the used oscilloscope (HDO 6104 by LeCroy) provides four channels and due to the symmetry of the three-phase system, waveforms with practically same shapes result for the three phases. Therefore, a second measurement was carried out exclusively for voltages and currents of phase a. This second measurement comprises the input voltage v_{an} of the primary-side half-bridge of phase a, the phase-to-neutral voltage v_a, the grid current i_a, and the secondary-side transformer current i_{TA}.[6] Fig. 19(b) shows the measured waveforms. Since the primary-side switching stage is operated using the clamping method described in [42], the shown waveform of v_{an} results, i.e., after a $120°$ sector of the grid period has elapsed, a clamping interval ($v_{an} = 0$) is enforced during a $60°$ sector of the grid period. Note that the clamping processes only affect the common mode voltage at the transformer and therefore have no effect on the primary-side transformer winding voltages v_{Ta}, v_{Tb}, v_{Tc}, cf. Section II and Fig. 3. The rms values of the four measured waveforms, as calculated by the oscilloscope over a grid period, are displayed at the bottom of the figure. On closer inspection, it can be seen that i_a is leading the grid voltage v_a by approximately $10°$. This capacitive reactive power requirement is caused by the filter capacitors [e.g. C_a in Fig. 1(a)] and the dc-blocking capacitors C_s of the iYR.

Fig. 19(c) depicts measured waveforms for operation with conventional modulation at OC1. The waveforms of v_{an}, v_a, and i_a are practically identical to the waveforms measured in Fig. 19(b). The THD of i_a is $4.0\,\%$. The measurement result of i_{TA} reveals a slightly larger envelope compared to the result in Fig. 19(b), which is also confirmed by the increased rms value ($7.87\,A$ instead of $6.25\,A$).

Fig. 19(d) shows the measurement result for operation with suboptimal modulation at OC3. There, i_a and v_a are almost in phase. The rms value of i_{TA} is $15.8\,A$.

[5] Due to the comparatively low value of L of $14\,\mu H$, it may be possible to optimize the transformer so that its leakage inductance realizes the entire required series inductance. In such a case, the additional inductance connected in series to the transformer could be omitted.

[6] Since the additionally used series inductors used to realize the total inductance L of the iYR are placed on the secondary side, the secondary-side current was measured. In this way, minor deviations in the inductor current as caused by the magnetizing current of the transformer can be further reduced. Since the turns ratio of the transformer is $n = 1$ and because the calculation does not take the magnetizing current of the transformer into account, the measured secondary-side transformer current can be directly compared to the calculated primary-side transformer current.

In total, six measurements such as those shown in Fig. 19 were carried out, i.e. for OC1, OC2, and OC3 and for the conventional and suboptimal modulation schemes. The sampling time of the recorded waveforms is 2 ns and the measurement duration is 50 ms (25 million samples per measured waveform). The rms values of i_{TA} over a grid period ($I_{\mathrm{TA,rms}}$), the THD values of i_{a}, and the power factors in phase a were calculated in MATLAB. Based on the assumption of three-phase symmetry, the rms value of $\langle I_{\mathrm{TABC,rms}} \rangle_{T_{\mathrm{g}}}$ can be calculated according to:

$$\langle I_{\mathrm{TABC,rms}} \rangle_{T_{\mathrm{g}}} = \sqrt{2} I_{\mathrm{TA,rms}}. \tag{45}$$

The above expression directly results from equation (34) in [39], since the rms values of the three phase currents are equal in a symmetrical three-phase system. In the context of the experimental verification, the use of (45) is justified by the fact that the three-phase laboratory voltage source used (Programmable AC Source 61509 by Chroma) generates a symmetrical three-phase voltage system and, apart from minor asymmetries due to component tolerances, the demonstrator also features three-phase symmetry. The results are listed in **Tab. III** and **Tab. IV** in comparison with calculated and simulated results. As can be seen from these tables, the measured and the simulated results are in very good agreement. However, slight differences appear in comparison to the calculation. As can be easily determined using circuit simulations, these differences are mainly due to the dead time of 140 ns, which is not considered in the calculation. Although the converter is operated without feedback control, low THD values are achieved even at low output power.

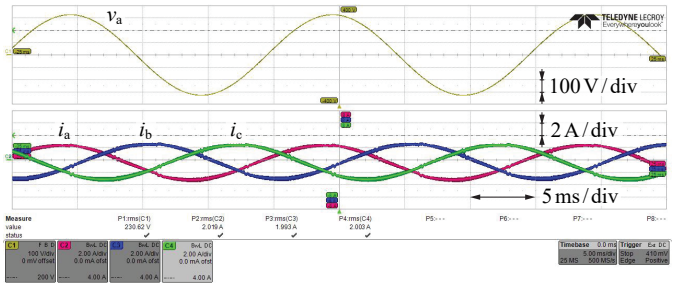

(a)

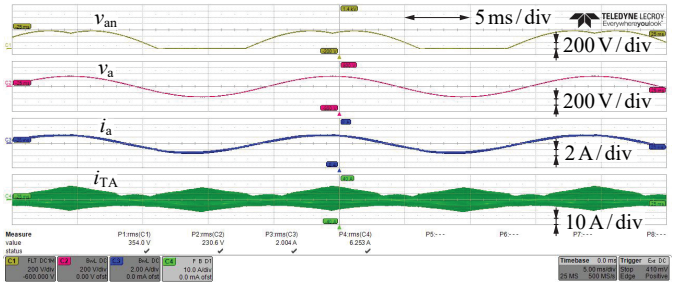

(b)

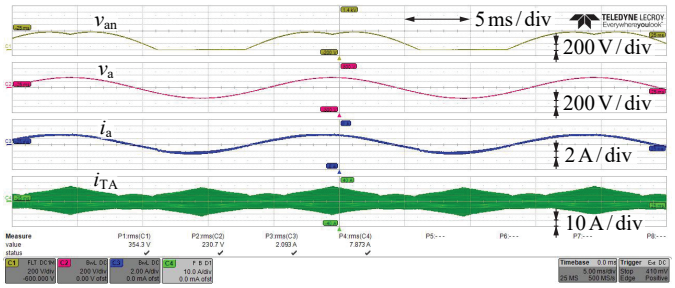

(c)

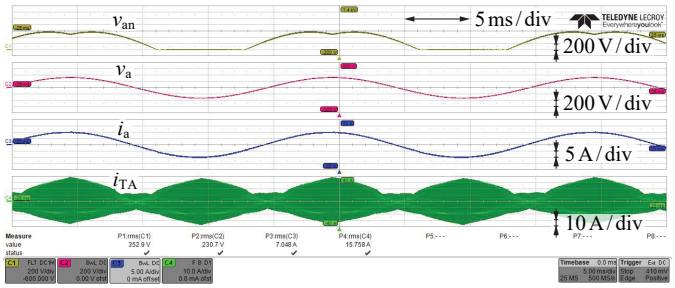

(d)

Fig. 19: Measured waveforms over 2.5 grid periods (= 50 ms): (a) Phase-to-neutral voltage v_{a} and phase currents $i_{\mathrm{a,b,c}}$ for suboptimal modulation and OC1; (b) waveforms of selected voltages and currents of phase a, for suboptimal modulation and OC1; (c) conventional modulation, OC1; (d) suboptimal modulation, OC3.

Fig. 20 provides a detailed view of the waveforms of v_{TA}, v_{TB}, v_{TC}, $v_{\mathrm{S'_a}}$ (the voltage across the primary-side switch $\mathrm{S'_a}$), and i_{TA} during a time period of 50 µs. For the operating point, OC1 and $\phi_{\mathrm{g}} = 10°$ were selected. Suboptimal modulation is used for **Fig. 20(a)** and **Fig. 20(b)**. The waveforms depicted in **Fig. 20(c)** result for conventional modulation. Note that a direct measurement of v_{TA}, v_{TB}, v_{TC} using differential voltage probes resulted in waveforms with pronounced superimposed oscillations. In order to avoid these oscillations, the voltages $v_{\mathrm{S'_A}}$, $v_{\mathrm{S'_B}}$, and $v_{\mathrm{S'_C}}$ at the three secondary-side low-side switches $\mathrm{S'_A}$, $\mathrm{S'_B}$, and $\mathrm{S'_C}$ were measured and the transformer voltages were determined in the oscilloscope using its maths channels:

$$v_{\mathrm{ABC0}} = \frac{v_{\mathrm{S'_A}} + v_{\mathrm{S'_B}} + v_{\mathrm{S'_C}}}{3}, \tag{46}$$

TABLE III: Conventional modulation: rms values of the transformer currents for the three operating conditions (OC) defined at the beginning of section VI and measured THD values and power factors, λ, for phase a.

OC	V_{dc}	I_{dc}	$\langle I_{\mathrm{TABC,rms,conv}} \rangle_{T_{\mathrm{g}}}$			THD	λ
			Calc.	Sim.	Meas.		
OC1	404 V	3.04 A	11.0 A	11.1 A	11.1 A	4.0 %	0.955
OC2	400 V	5.22 A	12.9 A	13.1 A	13.0 A	2.3 %	0.983
OC3	396 V	11.4 A	21.0 A	21.7 A	21.8 A	1.8 %	0.996

TABLE IV: Suboptimal modulation: rms values of the transformer currents for the three operating conditions (OC) defined at the beginning of section VI and measured THD values and power factors, λ, for phase a.

OC	V_{dc}	I_{dc}	$\langle I_{\mathrm{TABC,rms,subopt}} \rangle_{T_{\mathrm{g}}}$			THD	λ
			Calc.	Sim.	Meas.		
OC1	402 V	3.02 A	8.6 A	8.8 A	8.8 A	2.3 %	0.955
OC2	399 V	5.21 A	11.6 A	11.9 A	12.0 A	1.9 %	0.982
OC3	401 V	11.5 A	21.4 A	22.1 A	22.3 A	0.79 %	0.996

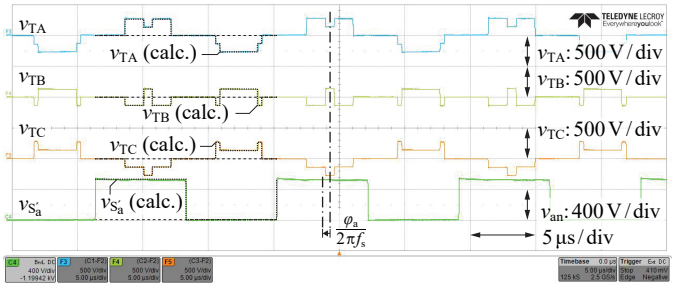

(a)

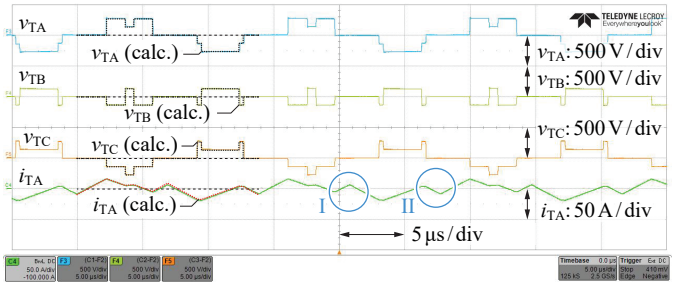

(b)

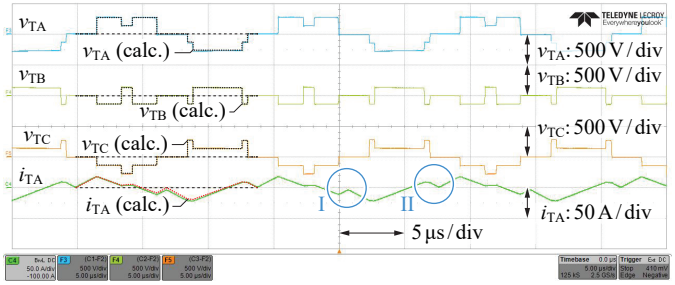

(c)

Fig. 20: Measured waveforms over a time period of $50\,\mu s$, for OC1 and $\phi_g = 10°$: (a), (b) suboptimal modulation; (c) conventional modulation. Calculated rms values over T_s at this operating point: $I_{TA,rms,subopt} = 8.7\,A$, $I_{TA,rms,conv} = 10.6\,A$.

$$v_{TA} = v_{S'_A} - v_{ABC0}, \quad v_{TB} = v_{S'_B} - v_{ABC0}, \quad v_{TC} = v_{S'_C} - v_{ABC0}. \tag{47}$$

Since the used oscilloscope provides four measurement channels, either $v_{S'_a}$ or i_{TA} was measured under the same operating conditions, see Fig. 20(a) and Fig. 20(b). The black dotted lines represent the calculated waveforms as determined with the method summarized in Section III-A. Apart from minor deviations, the calculated and measured curves coincide. The deviations can be attributed to simplifications in the calculation, such as the neglected dead time and that the switching operations are assumed to be ideal.

At first sight, i_{TA} in Fig. 20(b) and Fig. 20(c) appear to have nearly the same waveforms with similar peak values, which may raise the question of why their rms values should be different. Nevertheless, with $8.7\,A$ (suboptimal modulation) and $10.6\,A$ (conventional modulation), the measured rms values of i_{TA} (determined over one *switching period*) are clearly different. This can be explained by the regions marked with I and II in Fig. 20(b) and Fig. 20(c). These regions show that i_{TA} has two zero crossings during $v_{TA} = 0$ for suboptimal modulation. Consequently, i_{TA} remains in the vicinity of zero during $v_{TA} = 0$, i.e. when no active power is generated. At the shown operating point, these additional zero crossings do not occur for the conventional modulation. There, i_{TA} deviates more significantly from zero, resulting in a higher rms value.

VII. Conclusion

In this paper, different modulation schemes for the iYR are optimized with the aid of SV analysis. The aim of this optimization is to identify a modulation scheme which, compared to an existing scheme, achieves reduced rms values of the transformer currents in the iYR. It is found that this optimization can be carried out similarly to what is known for DAB dc–dc converters, since the equivalent circuit diagram of the iYR in the SV representation is the same as that of the DAB converter. Compared to the DAB converter, however, the iYR is substantially more complex, which in the context of an analytical study based on closed formulas would lead to the necessity of distinguishing between a high number of different cases. Therefore, a numerical method is presented that enables the calculation of the trajectories of the SVs of the currents and voltages in the iYR with low computational effort.

An extensive first optimization, which takes three degrees of freedom (DoFs) into account, shows that significant improvements in the transformer rms current value can be achieved in the low power range. However, the computed control parameters reveal characteristics with discontinuities, which can lead to difficulties in practice (e.g., excitation of parasitic oscillations). Therefore, in a second step, a target-oriented reduction of the DoFs is identified, leaving one DoF. The subsequent optimization performed on the basis of this DoF leads to a suboptimal modulation scheme with continuous control characteristics. In addition, apart from a minor part of the operating range, i.e. at low output voltage and low power, the suboptimal modulation scheme achieves practically the same improvements in the rms values of the transformer currents as the extensively optimized scheme. It should be emphasized that the control parameters $D_{(100)}$ and $D_{(110)}$ of the suboptimal modulation scheme depend on the level of the converted power. This is not the case for the conventional modulation scheme.

The experimental verification at three different operating points confirms the calculated results. For example, for the present hardware demonstrator (three-phase $400\,V$ rms line-to-line ac input voltage) for $V_{dc} = 400\,V$ and $P_{dc} = 20\,\%P_{nom} = 1.2\,kW$, the rms value of the transformer current SV can be reduced from $11.1\,A$ for conventional modulation to $8.8\,A$ for suboptimal modulation. Another interesting aspect of the iYR is that it achieves sinusoidal mains phase currents with low distortion in open-loop operation, e.g. a THD $\leq 4\,\%$ is measured for $V_{dc} = 400\,V$ and $P_{dc} = 1.2\,kW$.

This paper also demonstrates the general capabilities of SV analysis, which proves to be ideally suited for the optimization

of the modulation scheme for a complex three-phase PFC rectifier system and to investigate particular details related to the converter operation. One example of such a detail is the finding that the conventional modulation scheme can lead to fluctuating active and reactive power over a grid period, which is not the case for the optimized schemes. The methods presented in this paper also pave the way for further improvements, for example the development of a modulation scheme that minimizes the total losses (conduction and switching losses of the semiconductors, copper and core losses of the magnetic components). Other examples of possible future contributions are the allowance of a certain reactive power component, which leads to reduced rms values of the transformer currents, as shown in Fig. 13, and the utilization of further DoFs, such as an alternative control of the primary-side inverter with a duty cycle different to $50\,\%$.

APPENDIX

A. Converter Design

The two DoFs available for the design of the circuit are n and L. To determine the combination of n and L that leads to minimum conduction losses on average, the average efficiencies (considering only conduction losses) of the converter within the operating range specified in Tab. I are calculated for different values of n and L.

The presented results consider Y_{dsg} discrete and exponentially distributed values for n (between $n = 0.6$ and $n = 1.75$),

$$n = 10^{\left(\log_{10}(0.6)+\frac{y[\log_{10}(1.75)-\log_{10}(0.6)]}{Y_{\mathrm{dsg}}-1}\right)} \quad \forall \;\; y \in \mathbb{N}_0 \;\wedge\; y < Y_{\mathrm{dsg}}. \quad (48)$$

With regard to L, X_{dsg} discrete and linearly distributed values between $70\,\%L_{\max}(n)$ and $95\,\%L_{\max}(n)$ have been considered,

$$L(n) = L_{\max}(n)\left(0.7 + \frac{x(0.95-0.7)}{X_{\mathrm{dsg}}-1}\right) \quad \forall \;\; x \in \mathbb{N}_0 \;\wedge\; x < X_{\mathrm{dsg}}, \quad (49)$$

where $L_{\max}(n)$ denotes the maximum value of L with which the operating range specified in Tab. I can be covered for a given n. The value for $L_{\max}(n)$ is determined numerically using the method summarized in Subsection III-A for the considered (conventional or suboptimal) modulation scheme. The results presented in this Section have been determined for $X_{\mathrm{dsg}} \times Y_{\mathrm{dsg}} = 21 \times 21$ combinations of n and L.

The average efficiencies, $\overline{\eta_{\mathrm{cond}}}$, are calculated in the same way as described in Appendix A in [32] for $G_{\mathrm{dsg}} \times H_{\mathrm{dsg}} \times K_{\mathrm{dsg}} = 10 \times 4 \times 5$ different operating points. In this context, the operating points formed by all combinations of the linearly distributed values for V_{dc}, I_{dc}, and ϕ_{g},

$$V_{\mathrm{dc},g} = 200\,\mathrm{V} + \frac{g(750\,\mathrm{V}-200\,\mathrm{V})}{G_{\mathrm{dsg}}-1} \quad \forall \; g \in \mathbb{N}_0 \;\wedge\; g < G_{\mathrm{dsg}}, \quad (50)$$

$$I_{\mathrm{dc},h}(V_{\mathrm{dc},g}) = I_{\mathrm{dc,nom}}(V_{\mathrm{dc},g})\,\frac{h}{H_{\mathrm{dsg}}-1} \quad \forall \; h \in \mathbb{N}_0 \;\wedge\; h < H_{\mathrm{dsg}}, \quad (51)$$

$$\phi_{\mathrm{g},k} = 30^\circ\,\frac{k}{K_{\mathrm{dsg}}-1} \;\forall\; k \in \mathbb{N}_0 \;\wedge\; k < K_{\mathrm{dsg}}, \quad (52)$$

are considered. Note that $I_{\mathrm{dc,nom}}(V_{\mathrm{dc}})$ is related to the boundary of the operating range as defined in Tab. I,

$$I_{\mathrm{dc,nom}}(V_{\mathrm{dc}}) = \min\left(15\,\mathrm{A}, \frac{P_{\mathrm{nom}}}{V_{\mathrm{dc}}}\right). \quad (53)$$

The conduction losses are calculated according to

$$P_{\mathrm{cond}} = 3(R_{\mathrm{p}} + R_{\mathrm{tr}} + n^2 R_{\mathrm{s}})\left(\frac{\langle I_{\mathrm{Tabc,rms}}\rangle_{T_{\mathrm{s}}}(V_{\mathrm{dc}}, I_{\mathrm{dc}}, \phi_{\mathrm{g}})}{\sqrt{2}}\right)^2, \quad (54)$$

where $\langle I_{\mathrm{Tabc,rms}}\rangle_{T_{\mathrm{g}}}$ is substituted by (41) or (44), depending on the modulation scheme under consideration. R_{p} and R_{s} denote the on-state resistances of a primary- and secondary-side MOSFETs, respectively. With regard to the use of $1200\,\mathrm{V}$ SiC MOSFETs, these are set to $R_{\mathrm{s}} = 30\,\mathrm{m\Omega}$ and $R_{\mathrm{s}} = 30\,\mathrm{m\Omega}$. R_{tr} denotes the primary-side referenced copper resistance of the transformer windings, which is selected as $R_{\mathrm{tr}} = 10\,\mathrm{m\Omega}$.

Fig. 21(a) and **Fig. 21(b)** present the results of these calculations for conventional and suboptimal modulation, respectively. With conventional modulation, the optimal design is obtained for $n_{\mathrm{opt,conv}} = 0.784$ and $L_{\mathrm{opt,conv}} = 19.5\,\mu\mathrm{H}$. With suboptimal modulation, $n_{\mathrm{opt,conv}} = 0.921$ and $L_{\mathrm{opt,conv}} = 16.8\,\mu\mathrm{H}$ holds. In this paper, $n = 1$ was chosen in order to achieve a clear presentation of the results, i.e. to avoid possible confusion caused by a turns ratio unequal to 1. In addition, $L = 14\,\mu\mathrm{H}$ was chosen, which is close to the optimum inductance values determined for $n = 1$ in Fig. 21.

B. Operating Modes

The operating mode of the iYR is defined by the sequence of state changes of the inverter and the rectifier and this sequence is directly defined by the values of control parameters, cf. Fig. 4(a). For example, according to **Fig. 22(a)**, the hf ac voltage generated by the inverter in phase a, v_{Ta}, changes from $-157\,\mathrm{V}$ to $157\,\mathrm{V}$ at $t_\mu = 0$. At the same instant, also the other two half-bridges of the inverter change their switching state so that the inverter state changes from (000) to (111) at this point in time. Thereafter, the state of the rectifier changes from (011) to (001), etc.

If, for the operating point selected for Fig. 22(a), i.e., $V_{\mathrm{dc}} = 400\,\mathrm{V}$, $\phi_{\mathrm{g}} = 15^\circ$, $P = 5.8\,\mathrm{kW}$, and the remaining settings listed in Tab. I, the power is increased to $6.2\,\mathrm{kW}$, the waveforms shown in **Fig. 22(b)** results. When inspecting the waveforms v_{Ta} and v_{TA} at $t_\mu \approx T_{\mathrm{s}}/2$, it can be seen

that in Fig. 22(a) the switching of the rectifier from state (110) to state (100) occurs before the switching of the inverter from state (111) to state (000) takes place. This happens in reverse order in Fig. 22(b), where, at $t_\mu = T_s/2$, first the inverter switches from state (111) to state (000) and the rectifier switches thereafter from state (110) to state (100). Accordingly, the sequence of state changes of the inverter and the rectifier is different for Fig. 22(a) and Fig. 22(b). Thus, the operating mode of the converter is different as well.

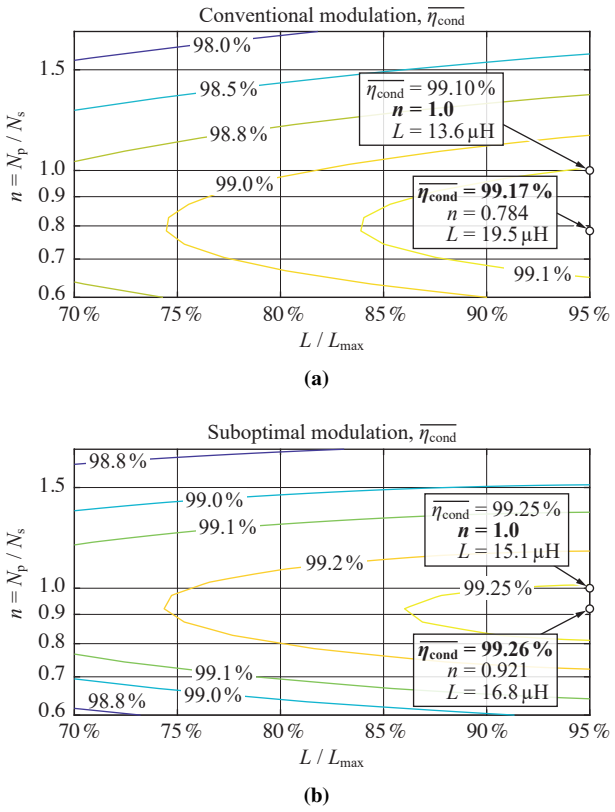

Fig. 21: Results for $\overline{\eta_{\text{cond}}}$: (a) conventional modulation scheme, (b) suboptimal modulation scheme. Marked are the optimal designs and suboptimal designs with $n = 1$.

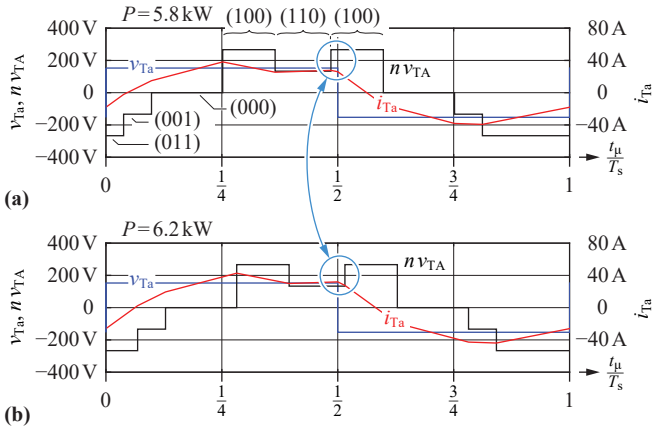

Fig. 22: Calculated waveforms of v_{Ta}, v_{TA}, and i_{Ta} for the conventional modulation scheme and the settings of Tab. I, $V_{\text{dc}} = 400\,\text{V}$, and $\phi_\text{g} = 15°$: (a) $P = 5.8\,\text{kW}$, (b) $P = 6.2\,\text{kW}$. The circled regions indicate the areas where the change of the power causes a mode change.

References

[1] D. Menzi, F. Krismer, T. Ohno, J. Huber, J. W. Kolar, and J. Everts, "Novel bidirectional single-stage isolated three-phase buck-boost PFC rectifier system," in *IEEE 38th Annu. Appl. Power Electron. Conf. Expo. (APEC)*, Orlando, FL, USA, Mar. 2013.

[2] Y. Li, Q. Sun, D. Qin, K. Cheng, and Z. Li, "Power control of a modular three-port solid-state transformer with three-phase unbalance regulation capabilities," *IEEE Access*, vol. 8, pp. 72 859–72 869, Apr. 2020.

[3] X. She, A. Q. Huang, and R. Burgos, "Review of solid-state transformer technologies and their application in power distribution systems," *IEEE Trans. Emerg. Sel. Topics Power Electron.*, vol. 1, no. 3, pp. 186–198, Sep. 2013.

[4] Y. Shi, R. Li, Y. Xue, and H. Li, "High-frequency-link-based grid-tied PV system with small DC-link capacitor and low-frequency ripple-free maximum power point tracking," *IEEE Trans. Power Electron.*, vol. 31, no. 1, pp. 328–339, Jan. 2016.

[5] L. Chen, A. Amirahmadi, Q. Zhang, N. Kutkut, and I. Batarseh, "Design and implementation of three-phase two-stage grid-connected module integrated converter," *IEEE Trans. Power Electron.*, vol. 29, no. 8, pp. 3881–3892, Aug. 2014.

[6] S. S. Shah, R. Narwal, S. Bhattacharya, A. Kanale, T.-H. Cheng, U. Mehrotra, A. Agarwal, B. J. Baliga, and D. C. Hopkins, "Optimized AC/DC dual active bridge converter using monolithic SiC bidirectional FET (BiDFET) for solar PV applications," in *IEEE Energy Convers. Congr. Expo. (ECCE)*, Vancouver, Canada, Oct. 2021, pp. 568–575.

[7] D. Sha and J. Chen, "Bidirectional three-phase high-frequency AC link DC–AC converter used for energy storage," *IET Power Electron.*, vol. 8, no. 12, pp. 2529–2536, Dec. 2015.

[8] A. Chambayil and S. Chattopadhyay, "A single-stage three phase bidirectional AC-DC DAB converter with multiphase boost interfaces," in *IEEE Int. Conf. Power Electron., Drives and Energy Syst. (PEDES)*, Jaipur, India, Dec. 2022, pp. 1–6.

[9] H. Radmanesh and M. Aeini, "A two-stage isolated AC-DC converter for more electric aircraft," in *11th Power Electron., Drive Syst., and Technol. Conf. (PEDSTC)*, Tehran, Iran, Feb. 2020, pp. 1–6.

[10] P. Sanjeev, N. P. Padhy, and P. Agarwal, "Peak energy management using renewable integrated DC microgrid," *IEEE Trans. Smart Grid*, vol. 9, no. 5, pp. 4906–4917, Sep. 2018.

[11] D. C. Erb, O. C. Onar, and A. Khaligh, "Bi-directional charging topologies for plug-in hybrid electric vehicles," in *IEEE 25th Annu. Appl. Power Electron. Conf. Expo. (APEC)*, Palm Springs, CA, USA, Feb. 2010, pp. 2066–2072.

[12] M. Yilmaz and P. T. Krein, "Review of battery charger topologies, charging power levels, and infrastructure for plug-in electric and hybrid vehicles," *IEEE Trans. Power Electron.*, vol. 28, no. 5, pp. 2151–2169, May 2013.

[13] E. I. Pool-Mazun, J. J. Sandoval, P. N. Enjeti, and I. J. Pitel, "An integrated solid-state transformer with high-frequency isolation for EV fast-charging applications," *IEEE Trans. Emerg. Sel. Topics Power Electron.*, vol. 1, no. 1, pp. 46–56, Jul. 2020.

[14] D. Menzi, D. Bortis, and J. W. Kolar, "Three-phase two-phase-clamped boost-buck unity power factor rectifier employing novel variable DC link voltage input current control," in *IEEE 2nd Int. Power Electron. and Appl. Conf. and Expo. (PEAC)*, Shenzhen, China, Nov. 2018, pp. 1–8.

[15] S. Inoue and H. Akagi, "A bidirectional DC–DC converter for an energy storage system with galvanic isolation," *IEEE Trans. Power Electron.*, vol. 22, no. 6, pp. 2299–2306, Nov. 2007.

[16] R. Huang and S. K. Mazumder, "A soft-switching scheme for an isolated DC/DC converter with pulsating DC output for a three-phase high-frequency-link PWM converter," *IEEE Trans. Power Electron.*, vol. 24, no. 10, pp. 2276–2288, Oct. 2009.

[17] L. Jia and S. K. Mazumder, "A loss-mitigating scheme for DC/pulsating-DC converter of a high-frequency-link system," *IEEE Trans. Ind. Electron.*, vol. 59, no. 12, pp. 4537–4544, Dec. 2012.

[18] K. Vangen, T. Melaa, and A. K. Ådnanes, "Soft-switched high-frequency, high power DC/AC converter with IGBT," in *IEEE 23rd Annu. Power Electron. Spec. Conf. (PESC)*, vol. 1, Toledo, Spain, June/Jul. 1992, pp. 26–33.

[19] J. Kan, S. Xie, Y. Wu, Y. Tang, Z. Yao, and R. Chen, "High-frequency-link inverter using combined synchronous rectifiers," *IEEE Trans. Ind. Electron.*, vol. 61, no. 12, pp. 6769–6777, Dec. 2014.

[20] K. V. Iyer, R. Baranwal, and N. Mohan, "A high-frequency AC-link single-stage asymmetrical multilevel converter for grid integration of renewable energy systems," *IEEE Trans. Power Electron.*, vol. 32, no. 7, pp. 5087–5108, Jul. 2017.

[21] T. Chen, R. Yu, and A. Q. Huang, "A bidirectional isolated dual-phase-shift variable-frequency series resonant dual-active-bridge GaN AC–DC converter," *IEEE Trans. Ind. Electron.*, vol. 70, no. 4, pp. 3315–3325, Apr. 2023.

[22] Z. Yan, M. Jia, C. Zhang, and W. Wu, "An integration SPWM strategy for high-frequency link matrix converter with adaptive commutation in one step based on de-re-coupling idea," *IEEE Trans. Ind. Electron.*, vol. 59, no. 1, pp. 116–128, Jan. 2012.

[23] D. Das, N. Weise, K. Basu, R. Baranwal, and N. Mohan, "A bidirectional soft-switched DAB-based single-stage three-phase AC–DC converter for V2G application," *IEEE Trans. Transport. Electrific.*, vol. 5, no. 1, pp. 186–199, Mar. 2019.

[24] K. Shigeuchi, J. Xu, N. Shimosato, and Y. Sato, "A modulation method to realize sinusoidal line current for bidirectional isolated three-phase AC/DC dual-active-bridge converter based on matrix converter," *IEEE Trans. Power Electron.*, vol. 36, no. 5, pp. 6015–6029, May 2021.

[25] L. Gu and K. Jin, "A three-phase isolated bidirectional AC/DC converter and its modified SPWM algorithm," *IEEE Trans. Power Electron.*, vol. 30, no. 10, pp. 5458–5468, Oct. 2015.

[26] J. W. Kolar, U. Drofenik, and F. C. Zach, "VIENNA rectifier II—a novel single-stage high-frequency isolated three-phase PWM rectifier system," *IEEE Trans. Ind. Electron.*, vol. 46, no. 4, pp. 674–691, 1999.

[27] B. J. D. Vermulst, J. L. Duarte, C. G. E. Wijnands, and E. A. Lomonova, "Quad-active-bridge single-stage bidirectional three-phase AC–DC converter with isolation: Introduction and optimized modulation," *IEEE Trans. Power Electron.*, vol. 32, no. 4, pp. 2546–2557, Apr. 2017.

[28] G. Castelino, K. Basu, and N. Mohan, "A novel three-phase bidirectional, isolated, single-stage, DAB-based AC-DC converter with open-loop power factor correction," in *IEEE Int. Conf. Power Electron., Drives and Energy Syst. (PEDES)*, Bengaluru, India, Dec. 2012.

[29] R. Baranwal, K. V. Iyer, K. Basu, G. F. Castelino, and N. Mohan, "A reduced switch count single-stage three-phase bidirectional rectifier with high-frequency isolation," *IEEE Trans. Power Electron.*, vol. 33, no. 11, pp. 9520–9541, Nov. 2018.

[30] D. Menzi, J. W. Kolar, H. Sarnago, Ó. Lucía, and J. E. Huber, "New 600V GaN single-stage isolated bidirectional 400V input three-phase PFC rectifier," in *IEEE Energy Convers. Congr. Expo. (ECCE)*, Nashville, TN, USA, Oct./Nov. 2023, pp. 6529–6531.

[31] N. Nain, I. Kovacevic-Badstuebner, J. Huber, U. Grossner, and J. W. Kolar, "Design aspects of three-phase current-source converter commutation cells with monolithic bidirectional GaN transistors," in *IEEE Energy Convers. Congr. Expo. (ECCE)*, Detroit, MI, USA, Oct. 2022.

[32] F. Krismer and J. W. Kolar, "Efficiency-optimized high-current dual active bridge converter for automotive applications," *IEEE Trans. Ind. Electron.*, vol. 59, no. 7, pp. 2745–2760, jul 2012. [Online]. Available: http://ieeexplore.ieee.org/document/5710417/

[33] J. Hu, "Modulation and dynamic control of intelligent dual-active-bridge converter based substations for flexible DC grids," Ph.D. dissertation, RWTH Aachen, Aachen, Germany, may 2019.

[34] G. Pfaff, A. Weschta, and A. F. Wick, "Design and experimental results of a brushless AC servo drive," *IEEE Trans. Ind. Appl.*, vol. IA-20, no. 4, pp. 814–821, July/Aug. 1984.

[35] H. W. van der Broeck, H.-C. Skudelny, and G. V. Stanke, "Analysis and realization of a pulsewidth modulator based on voltage space vectors," *IEEE Trans. Ind. Appl.*, vol. 24, no. 1, pp. 142–150, 1988.

[36] J. Holtz, "Pulse width modulation for electronic power conversion," in *Power Electronics and Variable Frequency Drives: Technology and Applications*, B. K. Bose, Ed. New York: IEEE Press, 1997, ch. 4, pp. 138–208.

[37] N. D. Weise, K. Basu, and N. Mohan, "Advanced modulation strategy for a three-phase AC-DC dual active bridge for V2G," in *Vehicle Power and Propulsion Conf.*, Chicago, IL, USA, Sept. 2011.

[38] J. W. Kolar, H. Ertl, and F. C. Zach, "Measurement and determination of the instantaneous power flow values in three-phase PWM converter systems based on the space vector calculus," in *Symposium on Measurement in Electrical and Electron. Power Syst.*, Zurich, Switzerland, Sept. 1989, pp. 1–21.

[39] ——, "Analytically closed optimization of the modulation method of a PWM rectifier system with a high pulse rate," in *Int. Conf. Power Electron. Intell. Motion (PCIM)*, Munich, Germany, June 1990, pp. 1–15.

[40] F. Krismer and J. W. Kolar, "Closed form solution for minimum conduction loss modulation of DAB converters," *IEEE Trans. Power Electron.*, vol. 27, no. 1, pp. 174–188, jan 2012. [Online]. Available: http://ieeexplore.ieee.org/document/5776689/

[41] D. G. Holmes and T. A. Lipo, *Pulse Width Modulation for Power Converters: Principles and Practice*. Wiley-IEEE Press, 2003, ch. 9 (Programmed Modulation Strategies), pp. 383–431.

[42] D. Menzi, A. Yang, S. Chhawchharia, S. Coday, and J. W. Kolar, "Novel three-phase electronic transformer," *IEEE Trans. Power Electron.*, vol. 39, no. 5, pp. 5027–5033, 2024.

This article has been accepted for publication in IEEE Journal of Emerging and Selected Topics in Power Electronics. This is the author's version which has not been fully edited and content may change prior to final publication. Citation information: DOI 10.1109/JESTPE.2024.3475826

Florian Krismer (Member, IEEE) received the Dipl.-Ing. M.Sc. degree in electrical engineering with specialization in automation and control technology from the Vienna University of Technology, Vienna, Austria, in 2004. In 2004, he joined the Power Electronic Systems Laboratory (PES) at the Swiss Federal Institute of Technology (ETH), Zurich, Switzerland, as a Ph.D. student and received his Ph.D. degree in 2010. He has been a Senior Researcher with PES and is currently a Senior Researcher with the Laboratory for High Power Electronic Systems (HPE) at ETH Zurich. Both at PES and at HPE he has co-supervised Ph.D. students and has continued with his research in the field of power electronics. He is the author or coauthor of numerous conference and peer-reviewed publications and has received eight IEEE Transactions and Conference Prize Paper Awards. His research interests include the analysis, design, and general optimization of power converter systems, e.g., the weight optimization of a bidirectional dc–dc converter for an airborne wind turbine. Furthermore, he conducts research related to the filtering of conducted electromagnetic emissions and collaborated in the littlebox-challenge with respect to the hardware realization.

David Menzi (Member, IEEE) received his B.Sc. and M.Sc. degree in Electrical Engineering and Information Technology at the Swiss Federal Institute of Technology (ETH), Zurich, Switzerland, in 2015 and 2017, respectively, and also spent a semester at the Royal Institute of Technology (KTH) in Stockholm, Sweden, as an exchange student. During his studies, he worked at ABB Medium Voltage Drives (MVD) in Turgi, Switzerland, as an intern and working student. He conducted his Ph.D. research in Electrical Engineering from 2018 to 2022 on bidirectional phase-modular three-phase buck-boost converter systems under the supervision of Prof. J.W. Kolar at the Power Electronic Systems Laboratory (PES) of ETH Zurich, and was awarded the EPCIA Student Award 2022 for his Ph.D. thesis. He is currently a Senior Researcher with PES at ETH Zurich and his research interests include, inter alia, ultra-compact and ultra-efficient three-phase ac-dc and dc-ac converter systems, extremely lightweight dc-dc converters for airborne applications, single-stage HF isolated ac-dc and ac-ac converters, and loss modelling of ferroelectric class II MLCCs.

Patrick Ziegler received his B.Sc. and M.Sc. degree in Electrical Engineering and Information Technology at the Swiss Federal Institute of Technology (ETH), Zurich, Switzerland, in 2021 and 2023, respectively, where he focused on power electronics. During his studies he worked on a SiC based motor controller for an electric race car for Formula Student. He is currently an electrical engineer at Varian Medical Systems, where he focuses on kV imaging.

Aobo Yang (Student Member, IEEE) received the B.Sc. degree in electrical engineering and automation with Tsinghua University, Beijing, China, in 2020, and the M.Sc. degree in electrical engineering and information technology with Swiss Federal Institute of Technology, Zurich, Switzerland, in 2023. Since January 2024, he has been working toward the Ph.D. degree with the Power Electronics Research Lab, University of Pennsylvania, Philadelphia, USA. He also spent a summer with Technical University of Kaiserslautern, Kaiserslautern, Germany, as a visiting student.

Johann W. Kolar (Fellow, IEEE) received his M.Sc. and Ph.D. degrees (summa cum laude - promotio sub auspiciis praesidentis rei publicae) from the University of Technology Vienna, Austria, in 1997 and 1999, respectively. Since 1984, he has been working as an independent researcher and international consultant in close collaboration with the Vienna University of Technology in the fields of power electronics, industrial electronics, and high-performance drive systems. He was appointed Assoc. Professor and Head of the Power Electronic Systems Laboratory at the Swiss Federal Institute of Technology (ETH) Zurich on Feb. 1, 2001, and was promoted to the rank of Full Prof. in 2004. Dr. Kolar has proposed numerous novel converter concepts, incl. the Vienna Rectifier, the Sparse Matrix Converter, and the Swiss Rectifier, has spearheaded the development of x-million rpm motors, and has pioneered fully automated multi-objective power electronics design procedures. He has supervised 90+ Ph.D. students to completion, has published 1000+ journal and conference papers and 4 book chapters, and has filed 200+ patents in the course of international industry research collaborations. He has presented 50+ educational seminars at leading international conferences and has served as IEEE PELS Distinguished Lecturer from 2012 – 2016. He has received 50 Transactions and Conference Prize Paper Awards, the 2014 IEEE Power Electronics Society R. David Middlebrook Achievement Award, the 2016 IEEE PEMC Council Award, the 2016 IEEE William E. Newell Power Electronics Award, the 2021 EPE Outstanding Achievement Award and 2 ETH Zurich Golden Owl Awards for excellence in teaching. He is a Fellow of the IEEE and was elected to the U.S. National Academy of Engineering as an international member in 2021. The focus of his current research is on ultra-compact/efficient WBG converter systems, ANN-based design procedures, Solid-State Transformers, ultra-high speed drives, bearingless motors, and life cycle analyses of power electronics systems.